NUMERICAL INVESTIGATION ON LAMINAR PULSATING FLOW THROUGH POROUS MEDIA

A Thesis
Presented to
The Academic Faculty

by

Sung-Min Kim

In Partial Fulfillment
of the Requirements for the Degree
Master of Science in the
School of Mechanical Engineering

Georgia Institute of Technology
May, 2008

NUMERICAL INVESTIGATION ON LAMINAR PULSATING FLOW THROUGH POROUS MEDIA

Approved by:

Dr. S. Mostafa Ghiaasiaan, co-Chair
School of Mechanical Engineering
Georgia Institute of Technology

Dr. S.I. Abdel-Khalik, co-Chair
School of Mechanical Engineering
Georgia Institute of Technology

Dr. Sheldon M. Jeter
School of Mechanical Engineering
Georgia Institute of Technology

Date Approved: 1/7/2008

To my parents Haengja Cheong and Daean Kim

ACKNOWLEDGEMENTS

First, thank you to my advisor, Dr. Ghiaasiaan, for his continued advice and mentoring over the years. He was considerate and very supportive all the time, I really appreciate what you have done for me both professionally and personally.

I would like to express gratitude to my co-advisor Dr. S.I. Abdel-Khalik, and Dr. Sheldon M. Jeter for their insightful suggestions and helpful comments. I would like to thank Dr. Yingjie Liu of Mathematics Department for helpful discussions and for sharing their breadth of expertise. I also would like to thank Dr. Youn J. Kim for his continuous trust and belief on me.

I am thankful to my first roommate Myeongsub Kim for helping me during my early years at Georgia Tech. I especially would like to thank Hannah Lee, who always supported me with love and warmth all through the journey of this master's degree. I thank her from the bottom of my heart.

Finally, I would like to thank my parents, my sister Kanghee Kim and my brother Sungmoo Kim, for their endless support and encouragement. They have always believed in me, and they have been patient with me. There is no way to repay them for their love. Without you this would not have been possible. Words can never express my gratitude for my family.

TABLE OF CONTENTS

LIST OF TABLES

LIST OF FIGURES

LIST OF SYMBOLS AND ABBREVIATIONS

Variables

a	Amplitude of velocity [m/s]
A	Constant
A_{pw}	Area of pore walls
B	Forchheimer coefficient [1/m]
$B_{xx,avg}$	Cycle-averaged Forchheimer coefficient [m^2]
$B_{xx,inst}$	Instantaneous Forchheimer coefficient along x direction for pulsating flow [m^2]
$B_{xx,st}$	Forchheimer coefficient along x direction for steady flow [m^2]
$\overline{\overline{B}}$	Forchheimer tensor [1/m]
D	Size of square rod [m]
f	Frequency [Hz]
H	Height of unit cell [m]
K	Permeability coefficient [m^2]
$K_{xx,avg}$	Cycle-averaged permeability coefficient [m^2]
$K_{xx,inst}$	Instantaneous permeability coefficient along x direction for pulsating flow [m^2]
$K_{xx,st}$	Permeability coefficient along x direction for steady flow [m^2]
$\overline{\overline{K}}$	Permeability tensor [m^2]
L	Length of unit cell [m]
p	Static pressure [N/m^2]

$\tilde{p}$	Spatial deviation pressure, $\tilde{p} = p - \langle p \rangle^f$ [N/m^2]
$\langle p \rangle^f$	Intrinsic volume-average fluid static pressure over V_f [N/m^2]
Re_L	Reynolds number based on a unit cell length L
Re_P	Pore-based Reynolds number
Re_{tran}	Critical Reynolds number for the transition from Darcy to Forchheimer flow
t	Time [s]
T	Period of oscillation [s]
u	Velocity [m/s]
U	Velocity [m/s]
$\tilde{\vec{u}}$	Spatial deviation velocity, $\tilde{\vec{u}} = \vec{u} - \langle \vec{u} \rangle^f$ [m/s]
$\langle \vec{u} \rangle$	Superficial volume-average fluid velocity over V [m/s]
$\langle \vec{u} \rangle^f$	Intrinsic volume-average fluid velocity over V_f [m/s]
V	Averaging control volume [m^3]
V_f	Fluid volume [m^3]
Δt	Time step size [s]

Greek Letters

ε	Porosity of medium
μ	Molecular viscosity [kg/m·s]
ν	Kinematic viscosity [m^2/s]
θ	Phase angle [deg]

ρ	Density [kg/m^3]
$\Delta\theta_V$	Phase shift of velocity [deg]
$\Delta\theta_P$	Phase shift of pressure [deg]
$\Delta\theta_{VP}$	Phase shift between velocity and pressure [deg]
ξ	Nondimensional pressure gradient

Subscripts

avg	Cycle-averaged value
i	Grid point index
in	Inlet
inst	Instantaneous value
m	Mean value
pt	Point
st	Steady state
tran	Transition from Darcy's flow to Forchheimer flow
xx	x direction

Superscripts

f	Fluid
n	Time step index

Others

I	Unit tensor
∂	Differential operator
∇	Gradient operator
$\rightarrow$	Vector
$=$	Tensor
$\langle\ \rangle$	Volume-averaged quantity

Abbreviations

CCD	Conservative second-order central difference scheme
CD	Nonconservative second-order central difference scheme
UD1	Nonconservative first-order upwind difference scheme
UD2	Nonconservative second-order upwind difference scheme
UD3	Nonconservative third-order upwind difference scheme

SUMMARY

In this investigation, the flow friction associated with laminar pulsating flows through porous media was numerically studied. The problem is of interest for understanding the regenerators of Stirling and pulse tube cryocoolers. Two-dimensional flow in a system composed of a number of unit cells of generic porous structures was simulated using a CFD tool, with sinusoidal variations of flow with time. Detailed numerical data representing the oscillating velocity and pressure variations for five different generic porous structure geometries in the porosity range of 0.64 to 0.84, with flow pulsation frequency of 40 Hz were obtained, and special attention was paid to the phase shift characteristics between the velocity and pressure waves. Based on these detailed numerical data, the standard unsteady volume-averaged momentum conservation equation for porous media was then applied in order to obtain the instantaneous as well as cycle-averaged permeability and Forchheimer coefficients. It was found that the cycle-averaged permeability coefficients were nearly the same as those for steady flow, but the cycle-averaged Forchheimer coefficients were about two times larger than those for steady flow. Significant phase lags were observed with respect to the volume-averaged velocity and pressure waves. The parametric trends representing the dependence of these phase lags on porosity and flow Reynolds number were discussed. The phase difference between pressure and velocity waves, which is important for pulse tube cryocooling, depended strongly on porosity and flow Reynolds number.

CHAPTER 1

INTRODUCTION

1.1 Background

Currently, the regenerative cryocoolers are widely used in a variety of applications, which require high performance and reliability. The regenerators that are found in Stirling and pulse tube cryocoolers are typically fine porous structures of various designs, which are constructed using wire mesh screens, sintered screens, metal foams, etc. Two relatively common regenerator filler materials, wire mesh screens and perforated disks, are shown in Figure 1. These screens and disks are packed into the regenerator tubes.

Cryocooler regeneration is a complicated and poorly-understood field. The utmost importance of regeneration for these systems is well-recognized, however. For an optimal design of a regenerative cryocooler, it is important to understand the complicated working mechanism of the cryocooler system at both component and system levels, and to improve the regenerator performance. In view of the importance of regeneration for cryocoolers, and the difficulty of detailed experimental measurements, this investigation is aimed at a theoretical investigation into the fundamental hydrodynamic phenomena associated with oscillating flow in porous media. Since porous structures of various configurations are used in regenerators, a generic porous structure is considered. Two-dimensional porous structure geometries composed of seven consecutive unit cells are simulated, and detailed numerical simulation are performed in order to understand the flow characteristics associated with pulsating laminar flow through porous media.

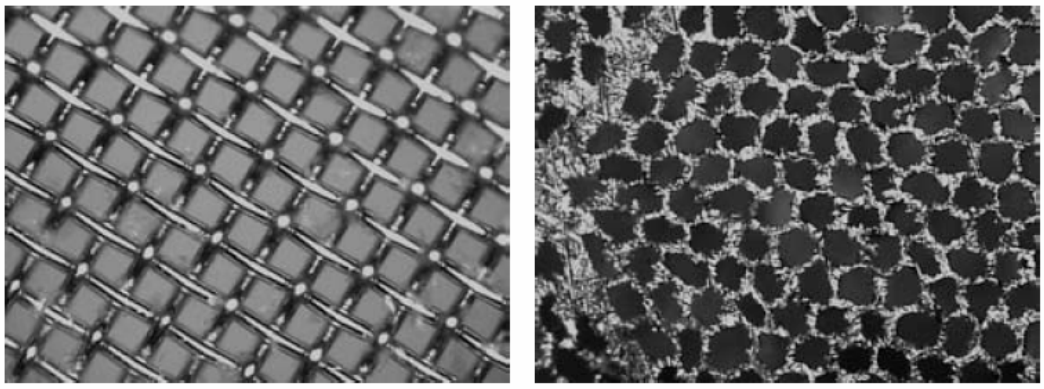

(a) Wire mesh (b) Perforated disk

Figure 1: The typical structure of a porous medium in the regenerators (200X magnification), adapted from Harvey [1]

1.2 Literature

The Forchheimer-extended Darcy equation for the incompressible flow through a homogeneous and isotropic porous medium has been widely used in experimental and numerical studies on convection heat transfer in a fully saturated porous media. For steady flow in a homogeneous porous medium, for example, one can write (Vafai and Tien [2], and Hsu and Cheng [3]).

$$-\nabla \langle p \rangle^{f} = \frac{\mu_f}{K} \langle \vec{u} \rangle + \rho_f B \left| \langle \vec{u} \rangle \right| \langle \vec{u} \rangle \tag{1}$$

where:

K = Permeability coefficient

B = Forchheimer coefficient

ρ_f = Fluid density

μ_f = Fluid molecular viscosity

$\langle p \rangle^f$ = Intrinsic volume-average fluid static pressure over a fluid volume V_f

$\langle \vec{u} \rangle$ = Superficial volume-average fluid velocity over an averaging control volume V

where the volume-averaged properties are defined as:

$$\langle \xi \rangle = \frac{1}{V} \int_{V_f} \xi \, dV \tag{1-a}$$

where ξ is any fluid property, V is the volume of a unit cell, and V_f is the volume of fluid within the unit cell.

Equation (1) is known as the Forchheimer-extended Darcy equation. When the velocity is sufficiently small, the Forchheimer term $\rho_f B \left| \langle \vec{u} \rangle \right| \langle \vec{u} \rangle$ of Equation (1) becomes negligibly small compared to the Forchheimer inertia term, and Equation (1) is reduced to the Darcy's law as follows,

$$-\nabla \langle p \rangle^f = \frac{\mu_f}{K} \langle \vec{u} \rangle \tag{2}$$

Thus, for very low Reynolds number flow through porous media, the pressure gradient is proportional to the velocity.

Figure 2 shows qualitatively the flow regimes in a homogeneous porous medium. It can be seen that there are three flow regimes in laminar flow. At extremely low flow rates, surface-interactive force dominates. This flow regime is typically of little interest to most applications. Without considering the surface-interactive force dominant flow regime which is only observed under very weak flows, the spectrum of laminar flow in porous media can be divided into Darcy's flow and Forchheimer flow regions [4]. The critical Reynolds number for the transition from Darcy's (viscous dominant) flow to Forchheimer (inertia dominant) flow, Re_{tran} , was examined by many researchers, for example, $\mathrm{Re}_{tran} \approx 4$ from Liu et al. [4], $1 < \mathrm{Re}_{tran} < 13$ from Coulaud et al. [5]. In this study, it is seen that the smooth transition around $\mathrm{Re}_{tran} \approx 7$ is observed from Figure 9.

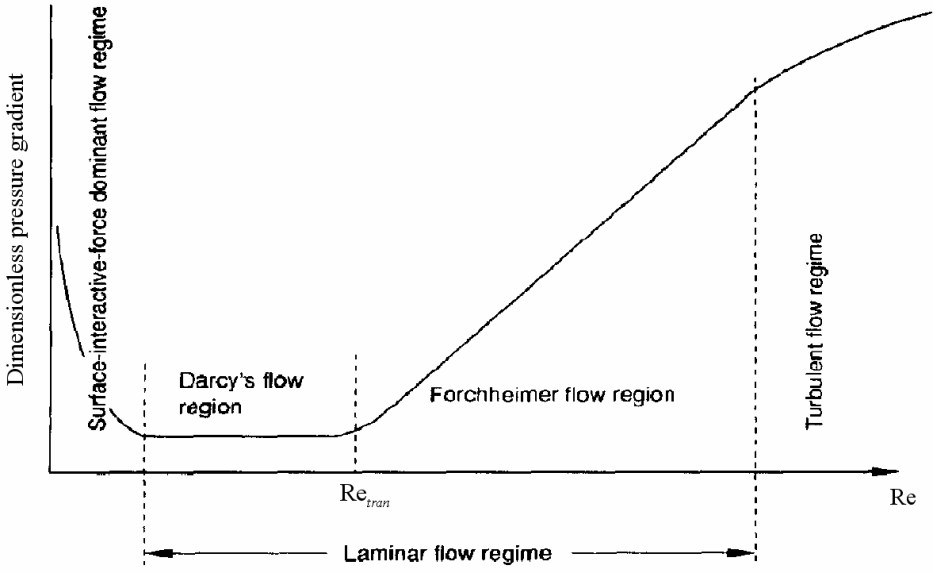

Figure 2: Flow regions in a porous medium in terms of Reynolds number, adapted from Liu et al. [4]

Equation (1) is phenomenological. The macroscopic governing equation for flow through a porous media can be rigorously derived by volume averaging the microscopic governing equation (the Navier-Stokes equation) over the representative element volume (REV), and the concept of volume-averaging theory (VAT) is widely used to analyze the flow in porous media. The theoretical basis for this and some other approaches is presented in a number of studies, namely, Vafai and Tien [2], Hsu and Cheng [3], Amiri and Vafai [6], Nakayama [7], Ochoa-Tapia and Whitaker [8], Kaviany [9], Nield and Bejan [10], and Whitaker [11]. When variation of fluid density and viscosity are considered to be negligible, and the porosity is assumed to be a constant, the volume averaged equation can be derived as:

$$\rho_f \left(\frac{\partial \left\langle \vec{u} \right\rangle^f}{\partial t} + \left\langle \vec{u} \right\rangle^f \cdot \left(\nabla \left\langle \vec{u} \right\rangle^f \right) \right) =$$

$$= -\nabla \left\langle p \right\rangle^f + \mu_f \nabla^2 \left\langle \vec{u} \right\rangle^f + \frac{1}{V_f} \int_{A_{pw}} \vec{n}_f \cdot \left(-\tilde{p} I + \mu_f \nabla \tilde{\vec{u}} \right) dA - \frac{\rho_f}{\varepsilon} \nabla \cdot \left\langle \tilde{\vec{u}} \tilde{\vec{u}} \right\rangle \tag{3}$$

where:

ρ_f = Fluid density

μ_f = Fluid molecular viscosity

I = Unit tensor

A_{pw} = Area of pore walls

$\tilde{p}$ = Spatial deviation pressure, $\tilde{p} = p - \left\langle p \right\rangle^f$

$\tilde{\vec{u}}$ = Spatial deviation velocity, $\tilde{\vec{u}} = \vec{u} - \left\langle \vec{u} \right\rangle^f$

This equation is evidently in need of closure relations in order to be solvable. In order to close the aforementioned volume-averaged equation, closure relations modeled by Vafai and Tien [2] and Whitaker [11] are used in this study, whereby:

$$\frac{1}{V_f}\int_A \vec{n}_f \cdot \left(-I\tilde{p} + \mu_f \nabla^2 \tilde{\vec{u}}\right) dA - \frac{\rho_f}{\varepsilon}\nabla \cdot \left\langle \tilde{\vec{u}}\tilde{\vec{u}} \right\rangle = -\frac{\varepsilon \mu_f}{\overline{\overline{K}}} \left\langle \vec{u} \right\rangle^f - \varepsilon^2 \rho_f \overline{\overline{B}} \cdot \left| \left\langle \vec{u} \right\rangle^f \right| \left\langle \vec{u} \right\rangle^f \tag{4}$$

By substituting Equation (4) into (3), the widely-used form of the volume-averaged momentum equations in terms of intrinsic velocity can be represented as (Hsu and Cheng [3], Vafai and Amiri [12], and Nakayama et al. [13]):

$$\rho_f \left(\frac{\partial \left\langle \vec{u} \right\rangle^f}{\partial t} + \left\langle \vec{u} \right\rangle^f \cdot \left(\nabla \left\langle \vec{u} \right\rangle^f \right) \right) =$$

$$= -\nabla \left\langle p \right\rangle^f + \mu_f \nabla^2 \left\langle \vec{u} \right\rangle^f - \frac{\varepsilon \mu_f}{\overline{\overline{K}}} \left\langle \vec{u} \right\rangle^f - \varepsilon^2 \rho_f \overline{\overline{B}} \cdot \left| \left\langle \vec{u} \right\rangle^f \right| \left\langle \vec{u} \right\rangle^f \tag{5}$$

where:

$\overline{\overline{K}}$ = Permeability tensor

$\overline{\overline{B}}$ = Forchheimer tensor

$\left\langle \vec{u} \right\rangle^f$ = Intrinsic volume-average fluid velocity over a fluid volume V_f

Two important points should be made about this equation. First, the equation in principle is

applicable only to quasi-steady (slow transient) conditions. Secondly, although the representation of the momentum equation in the above volume-averaged form is a major simplification, the elements of the permeability and Forchheimer coefficients still need to be specified. These can be found experimentally only for relatively simple configurations and boundary conditions. When experimental measurements are problematic, direct numerical simulation can be used, and this method is further discussed below.

In order to determine the macroscopic transport coefficients in porous media, many numerical studies have been performed using an infinite array of unit cells by implementing periodic boundary condition. The microscopic numerical results solved inside a periodic unit cell were used to obtain the macroscopic transport coefficients. Nakayama and Kuwahara [14] and Kuwahara et al. [15] modeled a porous medium in terms of obstacles arranged in a regular pattern, and obtained the macroscopic transport coefficients by solving the set of the microscopic governing equations using a periodic array of square rods and then integrating these microscopic results over a unit cell of the porous structure. In the study of Pedras and De Lemos [16], a numerical model was developed for turbulent flow in a porous medium represented by an infinite array of circular rods. The k-ε turbulence model was applied in this study, including an additional source term in the transport equations for k and ε. In order to investigate the effects of anisotropy, Nakayama et al. [17] used a bundle of rectangular cylinders to form an anisotropic porous media (see Figure 3), and determined the permeability and Forchheimer tensors, as well as the interfacial heat transfer coefficient, as functions of the macroscopic velocity vector and structural parameters.

As mentioned above, generic two-dimensional porous media are often represented

by an infinite array of parallel solid rods, subject to the cross-flow of the working fluid. This flow field configuration is evidently similar to flow over a surface equipped with pin fins. A large number of steady flow simulations have been performed to investigate the influences of pin fin cross-sectional shapes and arrangements on their pressure drop and heat transfer characteristics. Sahiti et al. [18] numerically studied the effect of the shape of pin cross-section on the pressure drop and heat transfer of six different pin fins. Sara [19] investigated the friction and thermal performance associated with flow through a rectangular channel with square cross-section pin fins attached over a flat surface. Jang et al. [20] studied the fluid flow and heat transfer over four rows of circular finned-tube heat exchangers with staggered arrangement.

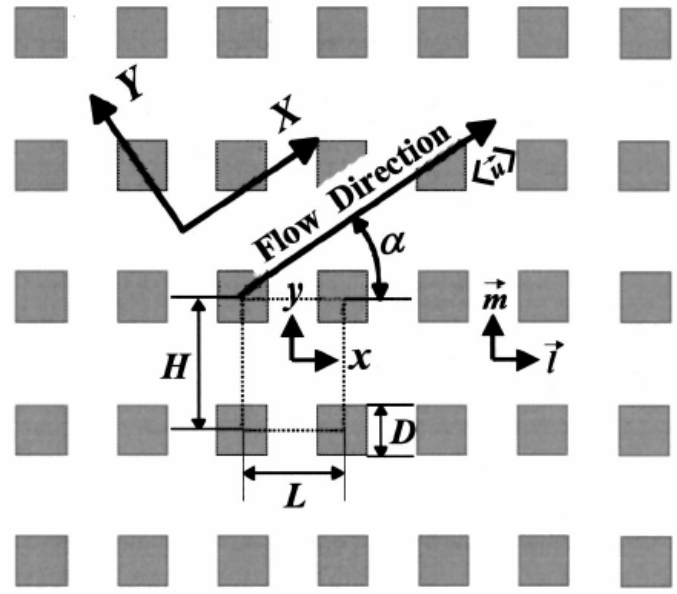

Figure 3: Coordinate system for periodic model of generic porous media, adapted from Nakayama et al. [17]

Some investigations have indeed considered modeling the flow through pin fins as flow in porous media. In this respect, steady, unidirectional and uniform flow over pin fins

along rectangular channel has been studied for estimating their permeability and Forchheimer coefficients. In the investigations of Kim et al. [21] and Jeng and Tzeng [22], for example, pin-fin heat sinks are modeled as a porous medium, and the pressure drop of pin fin heat sinks is obtained. The volume-averaged momentum equation is applied to the pin-fin heat sinks in order to obtain their macroscopic transport coefficients. Bundles of pin fins evidently constitute anisotropic porous media. However, for periodically fully developed flow, the pressure gradient along the flow direction is constant, and the flow pattern remains uniform. Accordingly, it has been argued that the results of steady, fully developed unidirectional flow through a uniform cross-section duct could be extended to fully developed flow through homogeneous porous media [23]. The above brief review of the literature dealing with the direct numerical simulation of flow in generic porous media shows that the previous studies have been focused on steady, unidirectional flow. Little attention has been paid to oscillating or periodic flow in porous media.

1.3 Objective and Approach

The objective of this study is to investigate by CFD simulations the flow friction associated with pulsating laminar flows through porous media. The goal is to compare the momentum transfer parameters representing steady and pulsating flow conditions, and thereby assess the adequacy of using steady-flow parameters in CFD-based simulation of pulsating flows in porous media. Five different generic porous structure geometries in the porosity range of 0.64 to 0.84 are analytically generated, and detailed numerical data representing the steady-flow and oscillating flow velocity and pressure variations along the flow direction are obtained by numerically solving the mass continuity and Navier-Stokes

equation using the finite-volume method. The oscillating flow simulations are performed at 40 Hz, in order to limit the scope of the parametric simulations. These detailed numerical simulations also predict a phase difference between the velocity and pressure waves. In separate CFD simulations, the instantaneous permeability and Forchheimer coefficients are calculated implicitly for the same porous structures using the volume-averaged momentum equation for flow in porous media using the finite-difference method. In the latter simulations, the cycle-averaged permeability and Forchheimer coefficients are iteratively adjusted so that the predictions of the porous-media based simulations match the predictions of the detailed, pore-level numerical simulations. This procedure thus leads to the calculation of cycle-averaged permeability and Forchheimer coefficients. The cycle-averaged permeability and Forchheimer coefficients of the pulsating flow are compared with those for steady flow. Special attention is also paid to the phase shift between the velocity and pressure waves, and the capability of the CFD-based analysis of the porous media flow predicting the phase shift.

CHAPTER 2

NUMERICAL METHOD

2.1 Computational Geometry

In this study, a two-dimensional generic porous structure is simulated, following the methodology of Nakayama and Kuwahara [14], Kuwahara et al. [15], and Nakayama et al. [17]. These authors were interested in steady and unidirectional flow, and therefore considered infinitely large porous media. The interest of this study is in pulsating flow. Accordingly, the porous structure is simulated by an array of seven square rods. In the aforementioned steady-flow investigations, the authors typically studied the flow details in a single unit cell, using periodic boundary conditions. For pulsating flow, however, a single unit cell is not sufficient due to the development of phase shift which makes simple periodic boundary conditions along the main flow direction irrelevant. It is for this reason that a row of six consecutive unit cells are used in this study. Figure 4 represents the computational domain, and a left to right main flow, along the x coordinate, is considered.

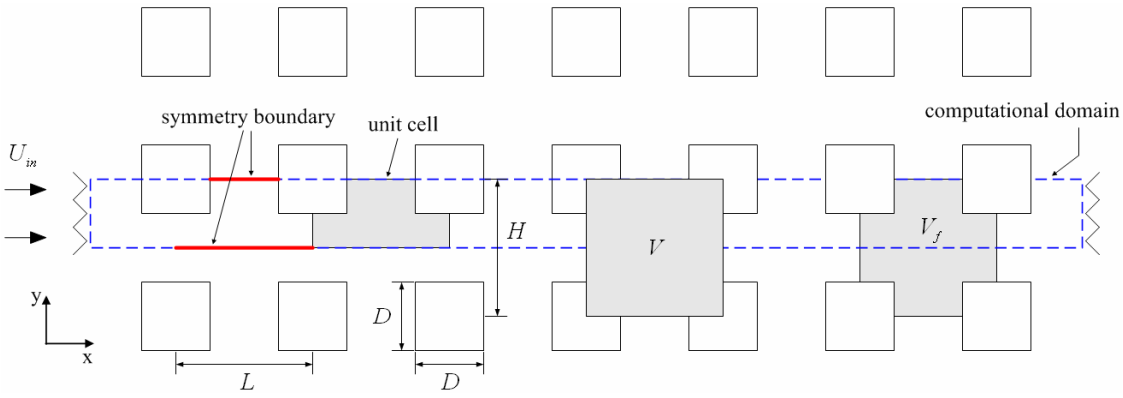

Figure 4: Computational domain with boundary conditions

The goal of this study is to understand the flow phenomena inside a porous structure, where the porous medium's inlet and exit effects are not present. An easy way to eliminate the inlet and exit effects is evidently, to simulate a finite number of unit cells, but consider in detail the flow phenomena in a unit cell where the inlet and exit effects are not present. Fortunately, past studies have shown that the entrance and exit effects only extend for a few unit cells in porous media [9]. Consequently, by using six unit cells in series, and investigating in detail the flow in the fifth unit cell, it is believed that the end effects are effectively eliminated in the simulation. The simulation results in fact support this argument, as will be shown later.

In order to reduce the number of grid points, the symmetry boundary condition is used at the top and bottom boundaries of unit cells, since the flow is symmetric around the x-axis.

The five generic porous structure geometries considered for analysis are shown in Figure 5. In all the porous structure geometries depicted in Figure 5, L=10 mm is assumed, and the ratio of H/L is fixed to one, therefore the porosity ε is found from:

$$\varepsilon = 1 - \left(\frac{D}{L}\right)^2 \tag{6}$$

The porosity of the structure is adjusted by varying D.

The five generic porous structures shown in Figure 5 have porosities of 0.84, 0.7975, 0.75, 0.6975 and 0.64. As mentioned earlier, the length of periodic unit cell L is fixed to 10 mm for all five porous structure geometries, and the size of square rod D is varied from 4 mm for ε=0.84, to 6 mm for ε=0.64. The Reynolds number range of 0.1 to

1000 is used for the simulation of the steady flow, where Reynolds number is defined based on a unit cell length L as:

$$\mathrm{Re}_L = \frac{\rho_f \left|\left\langle \vec{u} \right\rangle\right| L}{\mu_f} \tag{7}$$

where $\left\langle \vec{u} \right\rangle$ is the superficial volume-average fluid velocity.

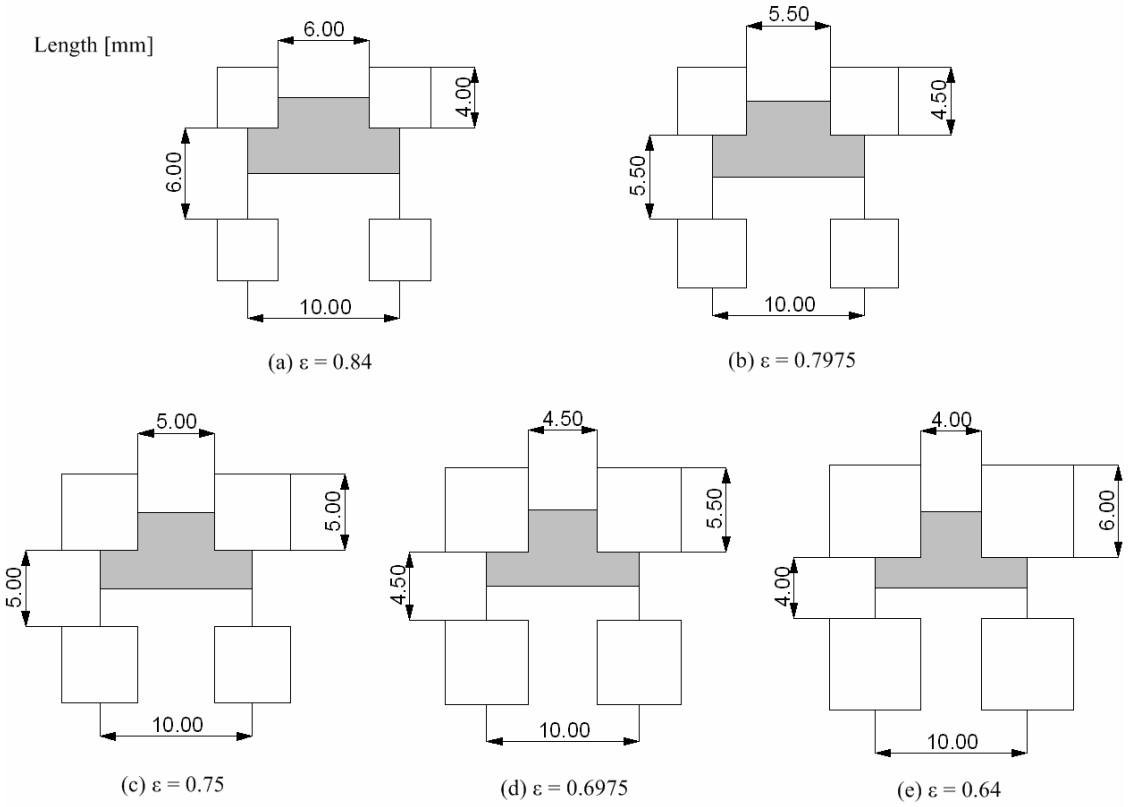

Figure 5: Different porous structure geometries showing a unit cell of continuous porous structures

Figure 6 shows a sample grid systems for the porous structure with $\varepsilon = 0.84$. A grid system that represents each unit cell with a 20×40 grid structure is used for $\varepsilon = 0.84$, and the same number of grids is maintained for all the other porous structures. Since the location of the inlet and outlet can affect the convergence as well as the accuracy of the simulations, the inlet and outlet are separated from the computational domain. The buffer zone length of $2L$ is used at the inlet. In order to eliminate the effect of the outflow boundary condition, a longer buffer zone length of $7L$ is used. It must be emphasized that the microscopic Navier-Stokes equation are solved for the instantaneous velocities and pressures along the flow direction through the six unit cells, namely, the domain between points 1 and 6 in Figure 6. Furthermore, the volume-average microscopic velocities and pressures representing each unit cell are used to solve the unsteady volume-averaged momentum equation, to be described shortly.

As mentioned before, two separate sets of conservation equations are solved for the system shown in Figure 6. The Navier-Stokes equations are solved for detailed pore-level simulations. These will be referred to as the microscopic equations. The results obtained with the microscopic equations will provide information that can be used for comparison with the results obtained from the solution of volume-average porous media-type equations. The latter equations will be referred to as the macroscopic equations.

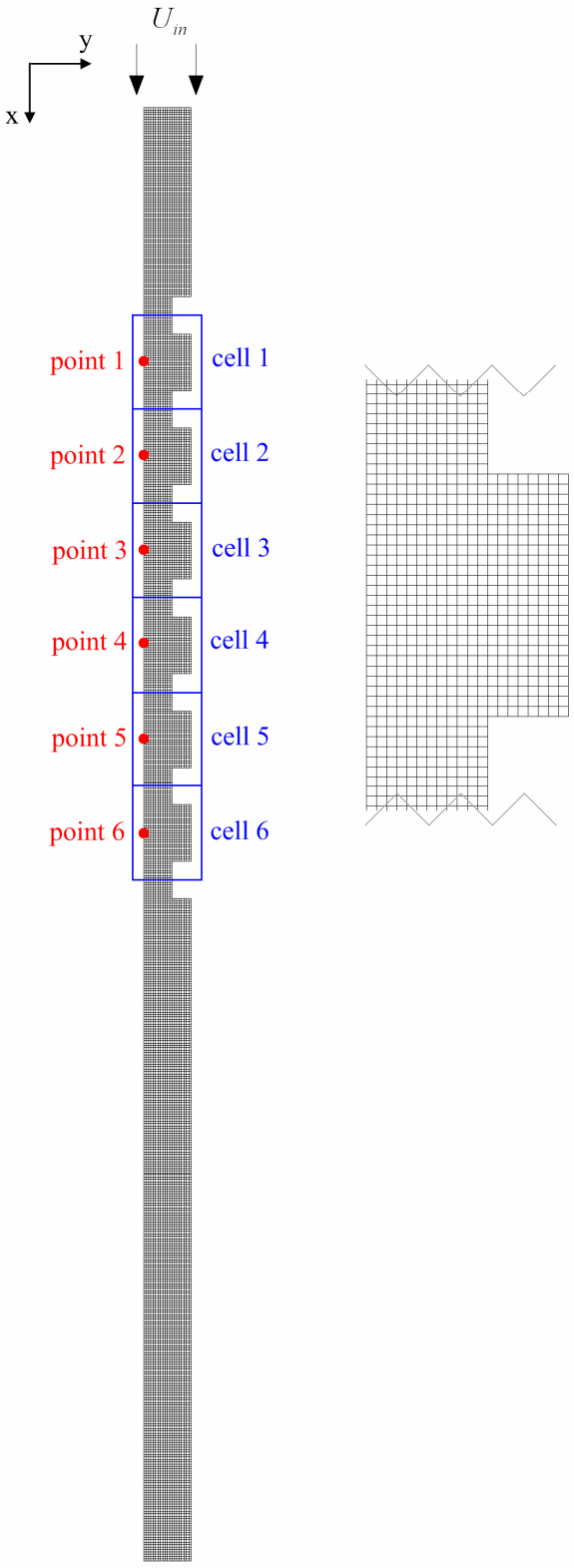

Figure 6: Sample grid system for $\varepsilon = 0.84$

2.2 Governing Equations for Microscopic Flow

It is assumed that the fluid is incompressible and has constant properties. The microscopic governing equations for unsteady laminar incompressible flow can be written as follows:

Conservation of mass equation:

$$\nabla \cdot \vec{u} = 0 \tag{8}$$

where $\vec{u}$ is velocity in vector form.

Conservation of momentum equation:

$$\frac{\partial \vec{u}}{\partial t} + \vec{u} \cdot \left(\nabla \vec{u} \right) = -\frac{1}{\rho_f} \nabla p + \nu_f \nabla^2 \vec{u} \tag{9}$$

where t = time, p = static pressure, ρ_f = density of the fluid, and ν_f = kinematic viscosity of the fluid.

2.3 Unsteady Volume-Averaged Momentum Equation (Macroscopic Flow)

The formulation of the macroscopic conservation equations here will be consistent with what is commonly used in porous media literatures (Vafai and Tien [2], Hsu and Cheng [3], Amiri and Vafai [6], Nakayama [7], Ochoa-Tapia and Whitaker [8], Kaviany

[9], Nield and Bejan [10], and Whitaker [11]). The superficial volume-average fluid velocity over an averaging control volume V is defined as:

$$\left\langle \vec{u} \right\rangle = \frac{1}{V} \int_{V_f} \vec{u}\, dV \tag{10}$$

where V and V_f denote the averaging control volume and the fluid volume contained within the averaging control volume, respectively. The intrinsic volume-average fluid velocity over the fluid volume V_f is defined as:

$$\left\langle \vec{u} \right\rangle^f = \frac{1}{V_f} \int_{V_f} \vec{u}\, dV \tag{11}$$

Therefore, the superficial and intrinsic volume averages are related by

$$\left\langle \vec{u} \right\rangle = \varepsilon \left\langle \vec{u} \right\rangle^f \tag{12}$$

where $\varepsilon = \frac{V_f}{V}$ is the volume fraction of the fluid-phase, or the porosity. In this study, V will represent the total volume of a unit cell, and V_f will refer to the total fluid volume contained in a unit cell (see Figure 4).

When variations of fluid density and viscosity are considered to be negligible, the widely-used form of the volume-averaged momentum equations in terms of intrinsic

velocity can be represented as (Hsu and Cheng [3], Vafai and Amiri [12], and Nakayama et al. [13]):

$$\rho_f \left(\frac{\partial \left\langle \vec{u} \right\rangle^f}{\partial t} + \left\langle \vec{u} \right\rangle^f \cdot \left(\nabla \left\langle \vec{u} \right\rangle^f \right) \right) =$$

$$= -\nabla \left\langle p \right\rangle^f + \mu_f \nabla^2 \left\langle \vec{u} \right\rangle^f - \frac{\varepsilon \mu_f}{\overline{\overline{K}}} \left\langle \vec{u} \right\rangle^f - \varepsilon^2 \rho_f \overline{\overline{B}} \cdot \left| \left\langle \vec{u} \right\rangle^f \right| \left\langle \vec{u} \right\rangle^f \tag{5}$$

The term $\frac{\varepsilon \mu_f}{\overline{\overline{K}}} \left\langle \vec{u} \right\rangle^f$ will be referred to as the Darcy term, which accounts for the viscous effect. This term depends on the geometry of the porous medium, and is the dominant loss term when the intrinsic average velocity $\left\langle \vec{u} \right\rangle^f$ is small. The term $\mu_f \nabla^2 \left\langle \vec{u} \right\rangle^f$ is the Brinkman term. This term also accounts for the viscous effects, but it is important in the interface between the porous medium and other solid boundaries, such as a wall or an adjacent fluid region. Away from such boundaries, the Brinkman term is usually negligible compared to the Darcy and Forchheimer terms. In this study, it was also noticed that the Brinkman term was negligibly small compared to the Darcy and Forchheimer terms. Finally, the term $\varepsilon^2 \rho_f \overline{\overline{B}} \cdot \left| \left\langle \vec{u} \right\rangle^f \right| \left\langle \vec{u} \right\rangle^f$ is referred to as the Forchheimer term, which accounts for the inertial effects, and becomes dominant when the intrinsic average velocity $\left\langle \vec{u} \right\rangle^f$ is large. Under macroscopically fully developed flow through a porous medium, the Darcy and Forchheimer terms depend only on the geometry of the porous medium, and the Forchheimer effect can be negligible when the flow rate through the porous medium

becomes vanishingly small.

The geometry of the porous structures shown in Figure 6 makes it clear that the x coordinate is a principle direction. As a result, when a pressure gradient in the x direction is imposed, the flow on a macroscopic scale will also be in the x direction only. Furthermore, with respect to a coordinate system that coincides with the principle directions, the tensors $\overline{\overline{K}}$ and $\overline{\overline{B}}$ are both diagonal. Thus, Equation (5) can be cast for flow in x direction as:

$$\rho_f \left(\frac{\partial \langle u_x \rangle^f}{\partial t} + \langle u_x \rangle^f \frac{\partial \langle u_x \rangle^f}{\partial x} \right) =$$

$$= -\frac{\partial \langle p \rangle^f}{\partial x} + \mu_f \frac{\partial^2 \langle u_x \rangle^f}{\partial x^2} - \frac{\varepsilon \mu_f}{K_{xx}} \langle u_x \rangle^f - \varepsilon^2 \rho_f B_{xx} \cdot \left| \langle u_x \rangle^f \right| \langle u_x \rangle^f \tag{13}$$

where K_{xx} and B_{xx} are x components of the diagonal tensors $\overline{\overline{K}}$ and $\overline{\overline{B}}$, respectively.

In case of steady macroscopic flow in x direction, the volume-averaged momentum equation can be cast in terms of the superficial (or Darcy) velocity,

$$0 = -\frac{\partial \langle p \rangle^f}{\partial x} - \left(\frac{\mu_f}{K_{xx,st}} \langle u_x \rangle + \rho_f B_{xx,st} \left| \langle u_x \rangle \right| \langle u_x \rangle \right) \tag{14}$$

where:

$K_{xx,st}$ = Permeability coefficient along x direction for steady flow

$B_{xx,st}$ = Forchheimer coefficient along x direction for steady flow

$\langle u_x \rangle$ = Superficial volume-average fluid velocity in x direction

Equation (14) is known as the Forchheimer-extended Darcy equation. This equation can be written in a nondimensional form as:

$$\xi = \frac{L^2}{K_{xx,st}\,\mathrm{Re}_L} + B_{xx,st}\,L \tag{15}$$

where the nondimensional pressure gradient ξ is defined as:

$$\xi = -\frac{\partial \langle p \rangle^f}{\partial x} \frac{L}{\rho_f \left| \langle u_x \rangle \right|^2} \tag{16}$$

For the case where the fluid velocity is sufficiently small, Equation (14) is reduced to the Dracy's law, displaying a simple linear relation between the flow velocity and pressure gradient along the flow direction:

$$-\frac{\partial \langle p \rangle^f}{\partial x} = \frac{\mu_f}{K_{xx,st}} \langle u_x \rangle \tag{17}$$

2.4 Numerical Algorithms

The algorithms used for the macroscopic-level equations are now discussed. The conservation equations for the microscopic flow are solved using the CFD code FLUENT

6.3 [24]. The CFD package options used will be discussed in Section 2.6. When the main flow direction is along x-axis, the unsteady volume-averaged momentum equation is [see Equation (13)]:

$$\rho_f \left(\frac{\partial \langle u_x \rangle^f}{\partial t} + \langle u_x \rangle^f \frac{\partial \langle u_x \rangle^f}{\partial x} \right) =$$

$$= -\frac{\partial \langle p \rangle^f}{\partial x} + \mu_f \frac{\partial^2 \langle u_x \rangle^f}{\partial x^2} - \frac{\varepsilon \mu_f}{K_{xx,inst}} \langle u_x \rangle^f - \varepsilon^2 \rho_f B_{xx,inst} \cdot \left| \langle u_x \rangle^f \right| \langle u_x \rangle^f \tag{18}$$

where:

$K_{xx,inst}$ = Instantaneous permeability coefficient along x direction for pulsating flow

$B_{xx,inst}$ = Instantaneous Forchheimer coefficient along x direction for pulsating flow

In order to obtain the instantaneous permeability and Forchheimer coefficients, the above equation is solved numerically using the finite difference method. The Backward in Time and Central in Space (BTCS) numerical scheme is selected for the solution of Equation (18). By denoting $\langle u_x \rangle^f$ and $\langle p \rangle^f$ as u_i^n and p_i^n, respectively, where n and i are time step and grid point indices, respectively, and considering the Taylor series expansions, it can be written as:

$$\frac{\partial \langle u_x \rangle^f}{\partial t} = \frac{u_i^n - u_i^{n-1}}{\Delta t} + O(\Delta t) \quad \text{: first-order backward difference} \tag{19}$$

$$\frac{\partial \langle p \rangle^f}{\partial x} = \frac{p_{i+1}^n - p_{i-1}^n}{2\Delta x} + O(\Delta x)^2 \quad \text{: second-order central difference} \tag{20}$$

$$\frac{\partial^2 \langle u_x \rangle^f}{\partial x^2} = \frac{u_{i+1}^n - 2u_i^n + u_{i-1}^n}{(\Delta x)^2} + O(\Delta x)^2 \qquad \text{: second-order central difference} \qquad (21)$$

For the convection term, $\langle u_x \rangle^f \left(\partial \langle u_x \rangle^f / \partial x \right)$, five different spatial discretization schemes were examined: conservative second-order central difference scheme (CCD), nonconservative second-order central difference scheme (CD), nonconservative first-order upwind difference scheme (UD1), nonconservative second-order upwind difference scheme (UD2), and nonconservative third-order upwind difference scheme (UD3).

$$\langle u_x \rangle^f \frac{\partial \langle u_x \rangle^f}{\partial x} = \frac{\frac{1}{2}\left(u_{i+1}^n\right)^2 - \frac{1}{2}\left(u_{i-1}^n\right)^2}{2\Delta x} + O(\Delta x)^2$$

: conservative second-order central difference (CCD) (22)

$$\langle u_x \rangle^f \frac{\partial \langle u_x \rangle^f}{\partial x} = u_i^n \frac{u_{i+1}^n - u_{i-1}^n}{2\Delta x} + O(\Delta x)^2$$

: nonconservative second-order central difference (CD) (23)

$$\langle u_x \rangle^f \frac{\partial \langle u_x \rangle^f}{\partial x} = u_i^n \frac{u_i^n - u_{i-1}^n}{\Delta x} + O(\Delta x)^1 \quad (u > 0)$$

: nonconservative first-order upwind difference (UD1) (24)

$$\langle u_x \rangle^f \frac{\partial \langle u_x \rangle^f}{\partial x} = u_i^n \frac{3u_i^n - 4u_{i-1}^n + u_{i-2}^n}{2\Delta x} + O(\Delta x)^2 \quad (u > 0)$$

: nonconservative second-order upwind difference (UD2) (25)

$$\langle u_x \rangle^f \frac{\partial \langle u_x \rangle^f}{\partial x} = u_i^n \frac{2u_{i+1}^n + 3u_i^n - 6u_{i-1}^n + u_{i-2}^n}{6\Delta x} + O(\Delta x)^3 \quad (u > 0)$$

: nonconservative third-order upwind difference (UD3) (26)

The comparison of different spatial discretization schemes for convection term will be discussed in Section 3.2. Based on these comparisions, nonconservative central difference scheme (CD) for convection term was selected for the solution of Equation (18).

By substituting Equations (19)-(21) and (23) into (18), the resulting finite difference equation will be

$$\rho_f \left(\frac{u_i^n - u_i^{n-1}}{\Delta t} + u_i^n \frac{u_{i+1}^n - u_{i-1}^n}{2\Delta x} \right) =$$

$$= -\frac{p_{i+1}^n - p_{i-1}^n}{2\Delta x} + \mu_f \frac{u_{i+1}^n - 2u_i^n + u_{i-1}^n}{(\Delta x)^2} - \frac{\varepsilon \mu_f}{K_{xx,inst}} u_i^n - \varepsilon^2 \rho_f B_{xx,inst} \cdot |u_i^n| u_i^n$$

$$+ O\left[(\Delta t), (\Delta x)^2 \right] \quad (27)$$

The BTCS implicit scheme applied here thus utilizes a first-order backward difference approximation for the time derivative and a second-order central difference approximation for the spatial derivatives. It is seen that the BTCS implicit scheme has a local accuracy of $O\left[(\Delta t), (\Delta x)^2 \right]$, and is unconditionally stable.

The calculation procedures for extracting the macroscopic flow permeability and Forchheimer coefficients from the microscopic-level solution are now discussed. The procedure for steady flow is self-evident, and needs no further discussion. For pulsating

flow, similar to the case of steady flow, when the mean flow velocity is very small, the Forchheimer term of Equation (27) can be neglected, and the permeability coefficient can be obtained. When the mean flow velocity is not vanishingly small, then the permeability and Forchheimer coefficients need to be considered both. The permeability can be treated as known, because it has by now been found from low-flow simulations, the Forchheimer coefficient can then be obtained from Equation (27).

The calculation procedure to obtain instantaneous permeability and Forchheimer coefficients is composed of the following five-step algorithm.

Step 1: obtain the intrinsic volume averaged values of u_i^n and p_i^n at $i=1$ to 6, and during n time snapshots covering two pulsation cycles from the microscopic-level solution results

Step 2: solve the following equation for the n time snapshots covering two pulsation cycles for low-flow simulations, and thereby obtain $K_{xx,inst}$

$$\rho_f\left(\frac{u_i^n-u_i^{n-1}}{\Delta t}+u_i^n\frac{u_{i+1}^n-u_{i-1}^n}{2\Delta x}\right)=$$

$$=-\frac{p_{i+1}^n-p_{i-1}^n}{2\Delta x}+\mu_f\frac{u_{i+1}^n-2u_i^n+u_{i-1}^n}{(\Delta x)^2}-\frac{\varepsilon\mu_f}{K_{xx,inst}}u_i^n \tag{28}$$

Step 3: obtain the cycle-averaged permeability coefficient, $K_{xx,avg}$

Step 4: solve the following equation for the n time snapshots covering two pulsation cycles for high-flow simulations, and thereby obtain $B_{xx,inst}$

$$\rho_f \left(\frac{u_i^n - u_i^{n-1}}{\Delta t} + u_i^n \frac{u_{i+1}^n - u_{i-1}^n}{2\Delta x} \right) =$$

$$= -\frac{p_{i+1}^n - p_{i-1}^n}{2\Delta x} + \mu_f \frac{u_{i+1}^n - 2u_i^n + u_{i-1}^n}{(\Delta x)^2} - \frac{\varepsilon \mu_f}{K_{xx,avg}} u_i^n - \varepsilon^2 \rho_f B_{xx,inst} \cdot |u_i^n| u_i^n \tag{29}$$

Step 5: obtain the cycle-averaged Forchheimer coefficient, $B_{xx,avg}$

The u^n, u^{n-1}, and p^n are already calculated values from the microscopic-level equations, thus the instantaneous permeability coefficient $K_{xx,inst}$ can be obtained from Step 2. In Step 3, the cycle-averaged permeability coefficient is defined as:

$$K_{xx,avg} = f \int_{t_o}^{t_o + \frac{1}{f}} K_{xx,inst} dt \tag{30}$$

By substituting $K_{xx,avg}$ into Equation (29), the instantaneous Forchheimer coefficient $B_{xx,inst}$ is numerically calculated from Step 4. Finally, the cycle-averaged Forchheimer coefficient can be obtained from:

$$B_{xx,avg} = f \int_{t_o}^{t_o + \frac{1}{f}} B_{xx,inst} dt \tag{31}$$

2.5 Boundary and Initial Conditions

The inlet boundary is located at a distance $2L$ upstream from the first square rod, where the velocity has a uniform profile. The no-slip boundary condition is applied on the wall. Since the geometric boundaries and physical conditions are symmetric along the x-axis, only half of the physical domain that represents the six unit cells is considered for the calculations (see Figure 6). That is, at the top and bottom faces of a unit cell, the normal gradients of all variables are prescribed as zero (the symmetry boundary condition). The outflow boundary is located at a distance $7L$ downstream from the last square rod where a zero-gradient is imposed for all dependent variables.

The Re_L range of 0.1 to 1000 is used for the simulation of the steady flow. The converged steady-state results are used as the initial values for the relevant unsteady calculations. For the simulation of oscillating flow with pulsation frequency of 40 Hz, the mean Reynolds numbers based on the mean Darcy velocity, $\mathrm{Re}_{m,L}$ =0.11 and 560, are selected for the calculation of the instantaneous permeability and Forchheimer coefficients, respectively. The sinusoidal velocity profile applied at the inlet of the computational domain in pulsating flow simulations is as follows

$$U_{in} = U_m \left[1 + a \sin\left(2\pi f t\right)\right] \tag{32}$$

where the amplitude of pulsating velocity a is 0.4, f = 40 Hz, and the mean value of pulsating flow velocities U_m of 0.00016 m/s and 0.818 m/s, which corresponds to the mean Reynolds numbers $\mathrm{Re}_{m,L}$ =0.11 and 560, are used for the calculation of the

instantaneous permeability and Forchheimer coefficients, respectively. The numerical simulations are conducted with air as the working fluid, assuming ρ_f = 1.225 kg/m^3 and μ_f = 1.7894×10^{-5} kg/(m·s). The sinusoidal pulsating area-averaged velocity at inlet boundary is implemented by a User Defined Function (UDF) of FLUENT 6.3 [24], and is described in Appendix A.

2.6 Solution Procedure for Microscopic-Level Equation

In order to obtain the volume-averaged velocities and pressures at each unit cell of generic porous structures, a user defined function (UDF) was coded in the C^{++} programming language (see Appendix A). The two-dimensional structured meshes for five different porous geometries were created by using the Gambit 2.2 software [25].

The microscopic governing equations along with the boundary and initial conditions are solved by using the CFD code FLUENT 6.3, which is based on the finite-volume method. The density-based Navier-Stokes coupled solution algorithm of FLUENT solves the governing equations of continuity and momentum simultaneously [24]. The first-order upwind discretization scheme is used to treat the convection terms. For the diffusion terms, the central difference scheme is used.

Detailed numerical data representing the oscillating velocity and pressure variations with flow pulsation frequency, 40 Hz, are obtained from the calculation of the microscopic governing equations. Then the volume-averaged velocities and pressures of each unit cell are used to numerically calculate the instantaneous as well as cycle-averaged permeability and Forchheimer coefficients from volume-averaged momentum equation, as described in Section 2.5. For this purpose, a program was coded in the programming

language, C^{++}. This program, which is depicted in Appendix B, solves the unsteady volume-averaged momentum equation implicitly by using the finite difference method with BTCS implicit scheme which, as described earlier, uses a second-order derivative in space and first-order derivative in time. The convergence of unsteady simulations is also checked by the aforementioned UDF.

CHAPTER 3

RESULTS AND DISCUSSION

3.1 Steady Flow

A convergence criterion of 10^{-6} was applied to the residuals of the continuity and momentum equations. Grid independence studies were carried out for the base case of ε=0.75 by checking the volume-averaged pressure gradient at Re_L=560. Two grid systems with 20×40 and 40×80 per unit cell were generated, and showed nearly identical velocity and pressure distributions (see Figure 7). The maximum difference of volume-averaged pressure gradient between the two grid systems was within 1%. For

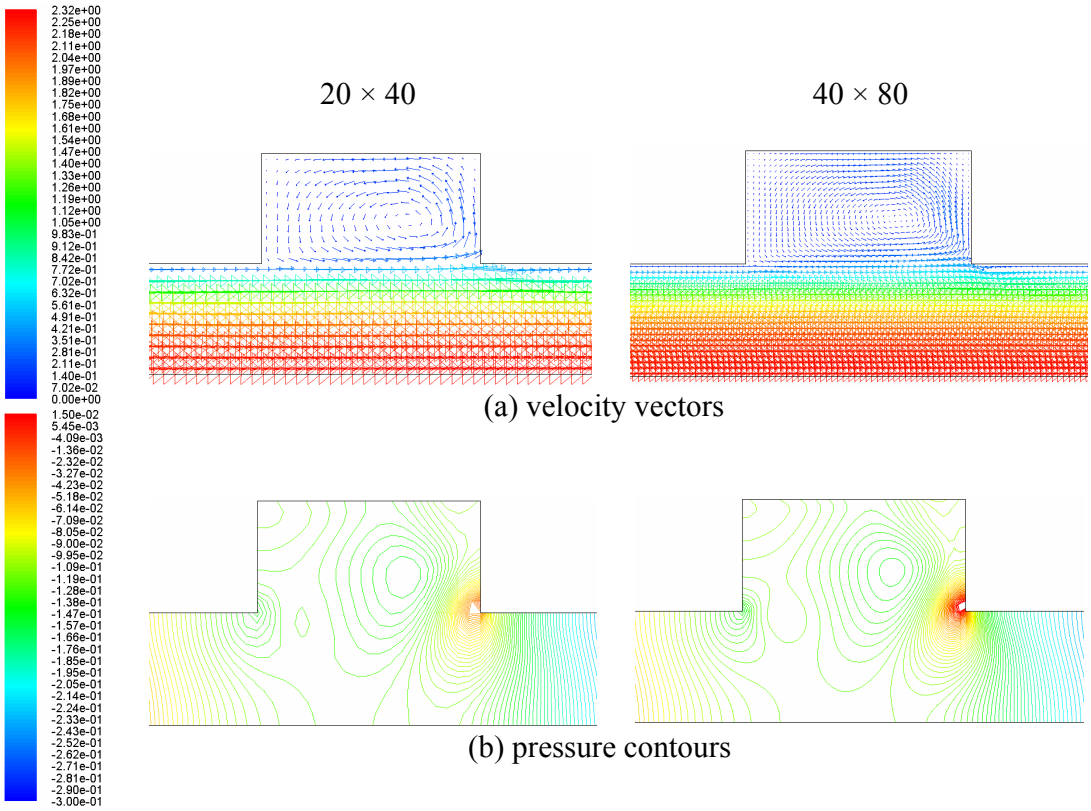

(a) velocity vectors

(b) pressure contours

Figure 7: Grid independence test for the base case of ε=0.75 with two grid systems

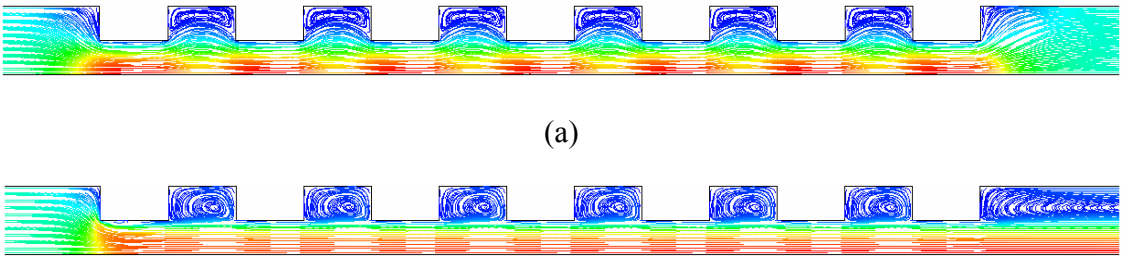

(a)

(b)

Figure 8: Steady-state streamline patterns for (a) Re_L=0.11, and (b) Re_L=560 in case of ε=0.75

calculation efficiency, a grid system with 20×40 per unit cell was chosen for all the subsequent simulations.

Figure 8 represents the typical steady-state streamline patterns in case of ε=0.75 for (a) Re_L=0.11 and (b) Re_L=560. To ensure hydrodynamically fully developed condition in the flow field, as explained before, the computational domain consists of six consecutive unit cells, and the inlet and outlet are sufficiently extended from the computational domain. It is seen that for the low Reynolds number flow, a small pair of vortices appear between the adjacent square rods. Since streamline patterns are nearly similar from the 1st to 6th unit cells, the flow is assumed to have attained a fully developed state. For the high Reynolds number flow, the position of the vortex center in the cavity is shifted slightly downstream. A large rotating vortex, which rotates in the counter-clockwise direction, exists in the cavity, and also a large recirculation vortex is formed behind the 6th unit cell.

The pressure drop characteristics along the flow direction are presented in term of the nondimensional pressure gradient ξ in Figure 9. The nondimensional pressure gradient undergoes a large change in the entrance region, and reaches an almost constant

value along the flow direction. At very low Reynolds numbers (Re_L <1), it is observed that the hydrodynamically fully developed regime is reached just after the 2nd unit cell. However, in case of high Reynolds numbers, the pressure gradient still varies slightly from the 3rd to 4th unit cells, and the change of pressure gradient from on unit cell to the next is decreased as the fully developed condition is reached further downstream. Similar trends have also been observed experimentally and numerically by many researchers, including Coulaud et al. [5], Sahiti et al. [18], Benarji et al. [26] and Raju and Narasimhan [27]. It was found that the change of nondimensional pressure gradient between the 4th and 5th unit cells is 0.04% and 1.7% for Re_L =35 and 980, respectively. Therefore, the flow after the 4th unit cell is considered to be fully developed, and the following results and observations are based on the 5th unit cell.

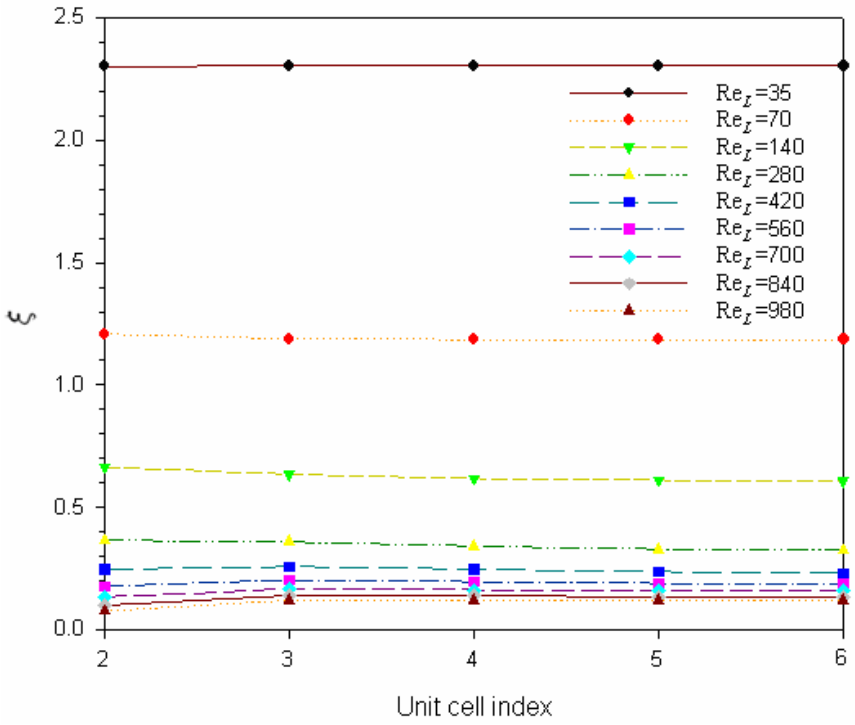

Figure 9: Nondimensional pressure gradient along the flow direction with Reynolds number for the steady flow

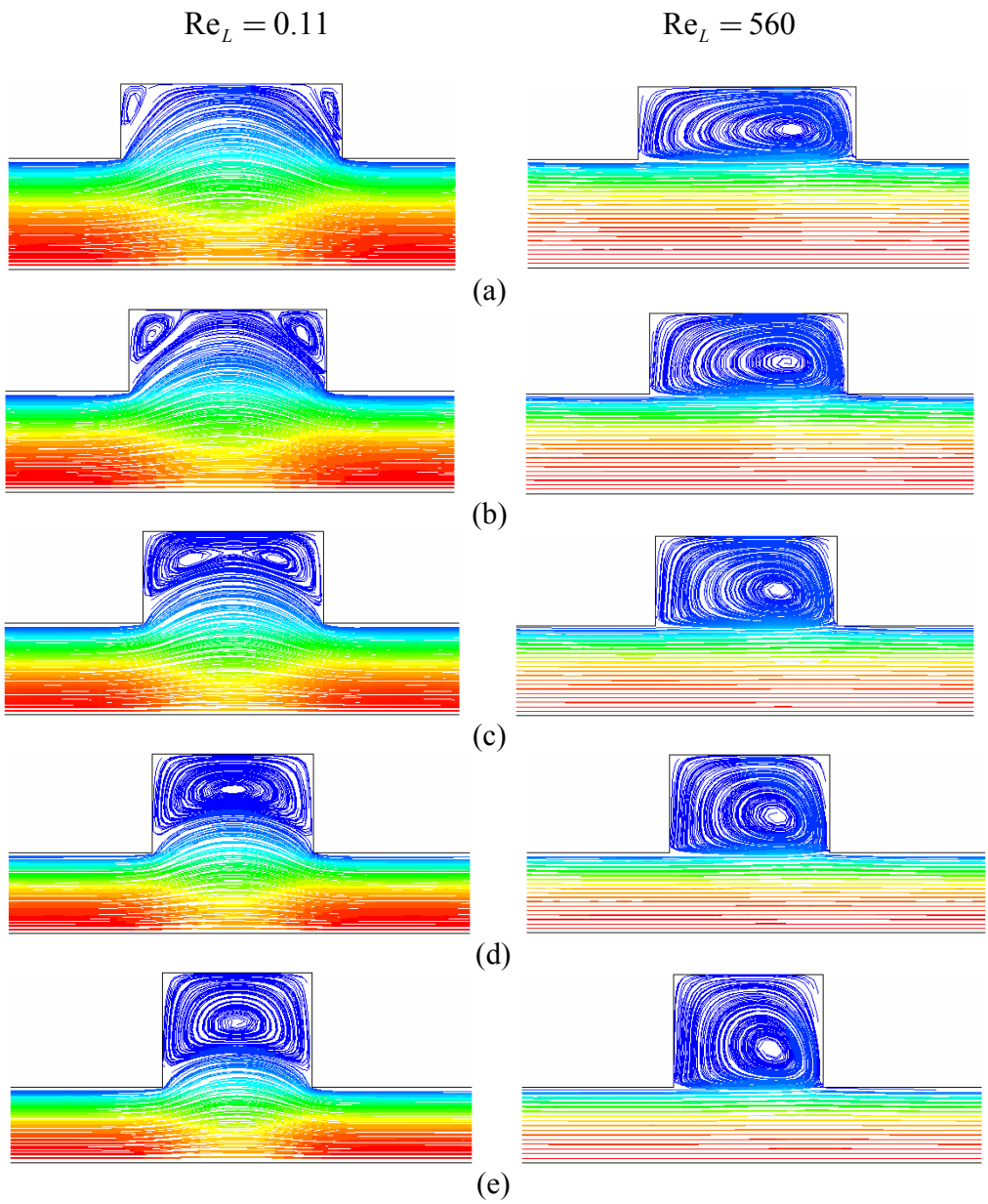

Figure 10: Detailed steady-state streamline patterns at the 5th unit cell for (a) ε=0.84, (b) ε=0.7975, (c) ε=0.75, (d) ε=0.6975, and (e) ε=0.64

Figure 10 shows the detailed steady-state streamline patterns at the 5th unit cell for all five different geometries. Since the pressure along the x-axis is larger than that at the cavity, the streamlines penetrate into the cavity. As the Reynolds number increases, the streamlines become parallel to the x-axis due to the increased inertia. For Re_L=0.11 and ε=0.84, there exists a small pair of vortices in the cavity. The vortices in the cavity are merged into a large rotating vortex with decreasing porosity ε. For Re_L=560, there is a large circulating vortex in the cavity, the position of whose center is moved downstream with increasing porosity. Detailed streamline patterns in similar cavities have also studied by Panfilov and Fourar [28] and Lucas et al. [29], with results that were generally consistent with the above observations.

In order to account for the viscous and inertia effects in porous region, Equation (14), which is a reduced form of the volume-averaged momentum equation for the steady flow, and also known as the Forchheimer-extended Darcy equation, is used. Figure 11 shows the nondimensional pressure gradient $\frac{\xi}{\mathrm{Re}_L}$ as a function of the Reynolds number. As the Reynolds number decreases and becomes vanishingly small, the inertia effect in porous region becomes negligible compared to the viscous effect, thus, for each ε, the nondimensional pressure gradient $\frac{\xi}{\mathrm{Re}_L}$ asymptotically reaches a constant value. That is, the flow in this region is controlled by Darcy's law, thus the permeability coefficient along x direction can be obtained from $\frac{\xi}{\mathrm{Re}_L} = \frac{L^2}{K_{xx,st}}$. For the same Reynolds number, the nondimensional pressure gradient increases as the porosity is decreased.

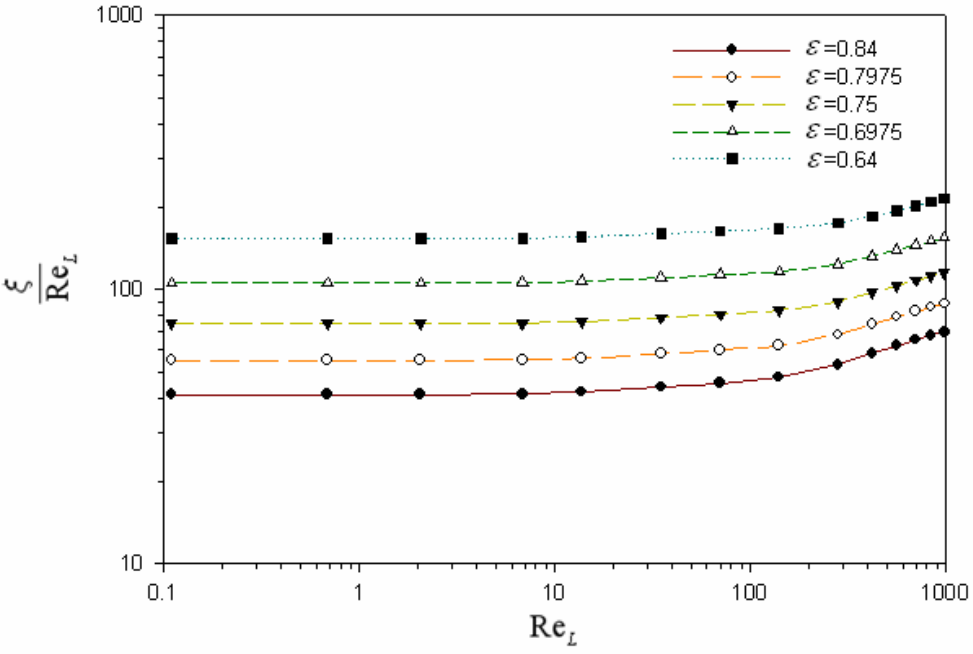

Figure 11: Nondimensional pressure gradient (permeability coefficient) as a function of Reynolds number for the steady flow

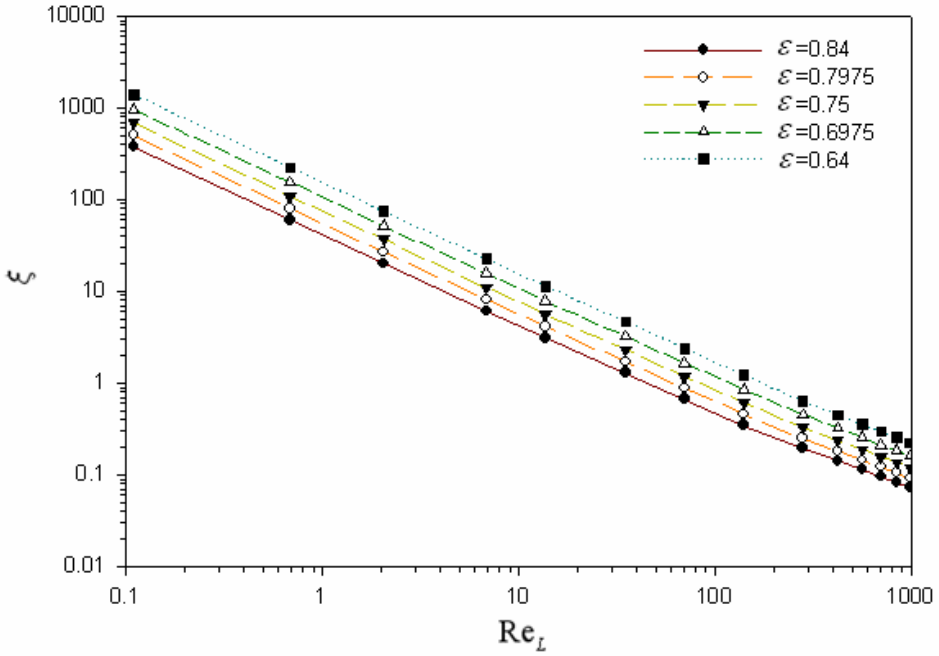

Figure 12: Nondimensional pressure gradient (Forchheimer coefficient) as a function of Reynolds number for the steady flow

At higher flow rates Darcy's law becomes inapplicable, and the flow is controlled by the Forchheimer-extended Darcy equation. As shown in Figure 12, the nondimensional pressure gradient ξ decreases with increasing Reynolds number, and it increases with increasing porosity. The x direction Forchheimer coefficient can be obtained from nondimensional pressure gradient $\xi = \frac{L^2}{K_{xx,st}\,\mathrm{Re}_L} + B_{xx,st}\,L$, shown in Figure 12. It is found that, as the Reynolds number increases beyond about 200, the Forchheimer term $B_{xx,st}\,L$ of Equation (15) becomes almost constant and independent of Reynolds number, as shown in Figure 13. The Forchheimer coefficient was determined by the interpolation of numerical data.

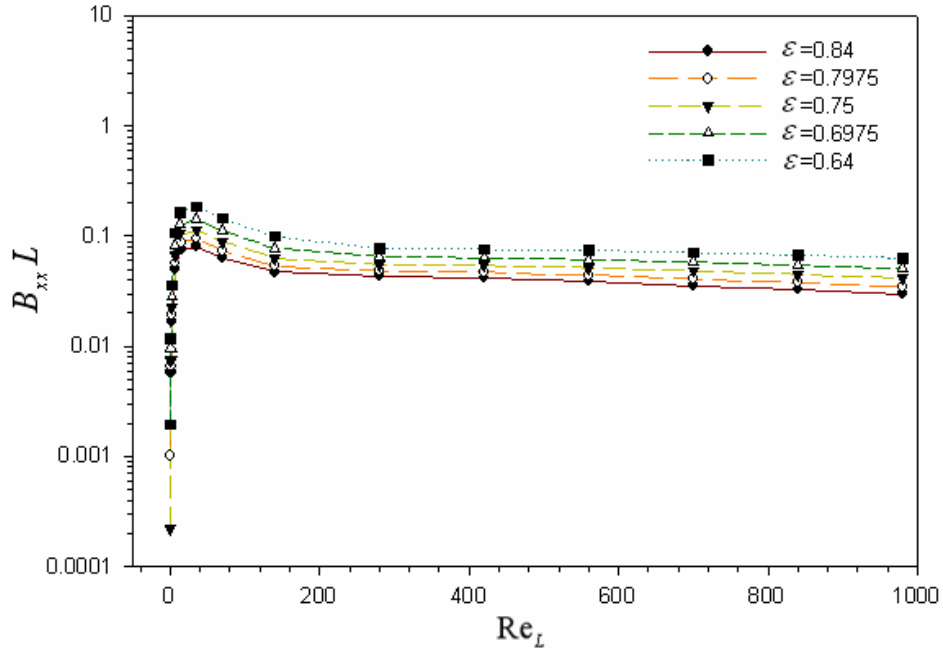

Figure 13: Forchheimer term as a function of Reynolds number for the steady flow

The permeability and Forchheimer coefficients for steady flow are shown in Table 1, and are compared with the results reported by Nakayama et al. [17]. The latter authors performed numerical simulations aimed at deriving closure relations for steady flow in generic porous media. Their definition of the generic porous media was similar to Figure 5(c). Calculated magnitude of permeability coefficient, $\frac{L^2}{K_{xx,st}}$=75, for ε=0.75, agrees well with $\frac{L^2}{K_{xx,st}}$=76 reported by Nakayama et al. [17], who also obtained the coefficient by numerical simulation. However, the value of Forchheimer coefficient, $B_{xx,st}L$=0.2, from [17], was four times larger than $B_{xx,st}L$=0.049 obtained in this study.

Table 1: Permeability and Forchheimer coefficients for steady flow

ε	$\frac{L^2}{K_{xx,st}}$	$B_{xx,st}L$
0.64	153	0.071
0.6975	105	0.058
0.75	75	0.049
0.7975	55	0.041
0.84	41	0.036

3.2 Pulsating Flow

For the calculation of unsteady pulsating flow parameters, the time derivatives are approximated by the second-order accurate implicit formulation. Pulsating flow

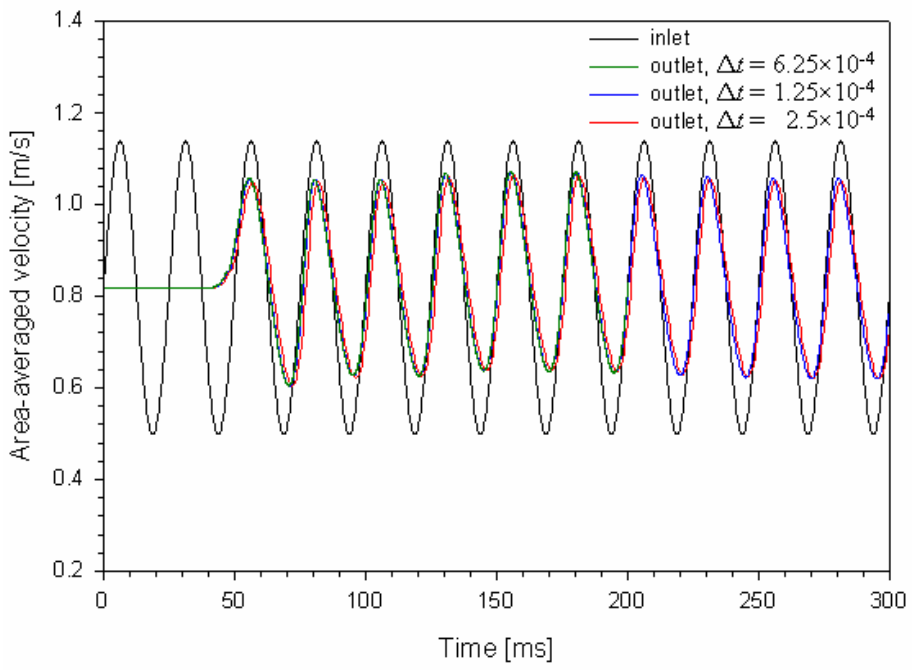

Figure 14: Time independence test for the base case of ε=0.75 with the grid size of 20 × 40 per unit cell

simulations are initiated from an assumed initial condition, and are continued until steady-pulsating conditions are achieved. The solutions of the steady flow served as the aforementioned initial conditions for the pulsating flow simulations. Similarly to the steady flow simulations, two grid systems with 20×40 and 40×80 nodes per unit cell were generated, and grid independence was investigated by checking the volume-averaged pressure gradients obtained with the two grid systems. It was observed that the maximum difference in volume-averaged pressure gradient between the two grid systems was 2.8% at the first unit cell. Additionally, the effect of the time step size was studied by using three time step sizes Δt=2.5×10^{-4} s (T/100), 1.25×10^{-4} s (T/200) and 6.25×10^{-4} s (T/400), in simulations where the period of oscillation T was 0.025 s. Figure 14 compares the instantaneous area-averaged velocities at inlet and outlet for the base case of ε=0.75 with a

grid size of 20×40 per unit cell, for the aforementioned three time step sizes. The results show that there is no significant difference among the model predictions for three time steps. The errors in mass conservation, which were defined as the percent difference of cycle-averaged velocities between inlet and outlet, were 1.01, 0.95, and 0.93% for $\Delta t = 2.5\times10^{-4}$ *s*, 1.25×10^{-4} *s*, and 6.25×10^{-5} *s*, respectively.

The time step size of 1.25×10^{-4} *s* (T/200) and a grid size of 20×40 per unit cell are used in the forthcoming calculations of unsteady pulsating flow. As mentioned earlier, pulsating flow simulations are started from an assumed initial condition, and are continued until the values of instantaneous velocities and pressures at Points 1 to 6 reach the cyclic steady state condition. In other words, all calculated quantities at t and $t+T$ at these two points must be exactly the same when cyclic steady state conditions are achieved. The instantaneous and volume-averaged velocities and pressures are monitored at points 1 to 6, namely the inlet and outlet, and continuously recorded for later calculation. Figure 15 represents the instantaneous velocities and pressures along the flow direction. These calculations have been carried out for each case with a time step size of 1.25×10^{-4} *s* (T/200), where the period of oscillation T is 0.025 *s*, up to 0.375 *s* of total simulation time. Although the calculations are continued during the total time of 0.375 *s*, the cyclic steady state solutions are obtained after 7 cycles of pulsation periods or 0.175 *s*. The convergence criterion was based on the relative error in the oscillating velocity component, which was required to be smaller than 10^{-3}. The relative errors of oscillating velocities were 7.1×10^{-5} and 1.8×10^{-4} at points 1 and 2, respectively. The relative errors of the oscillating pressures were 6.8×10^{-3} and 9.5×10^{-3} at points 1 and 2, respectively. Furthermore, the mass conservation for the computational domain was examined by calculating the percent

difference of cycle-averaged velocities between inlet and outlet. As shown in Table 2, for the case of $\mathrm{Re}_{m,L}$=0.11, the errors in mass conservation were less than 0.2%. However, for the high Reynolds number case, the errors in mass conservation increased with decreasing the porosity, and reached the maximum value of 1.7% for the case of ε=0.64.

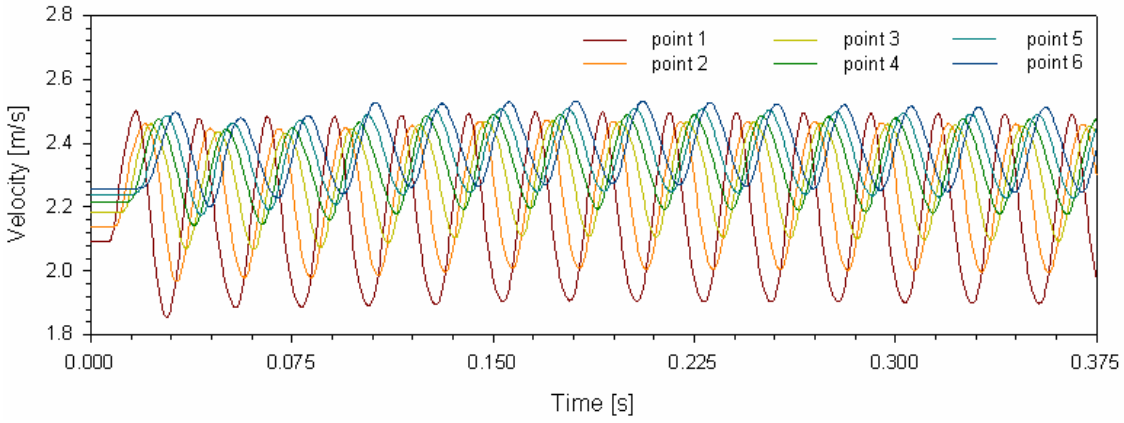

(a)

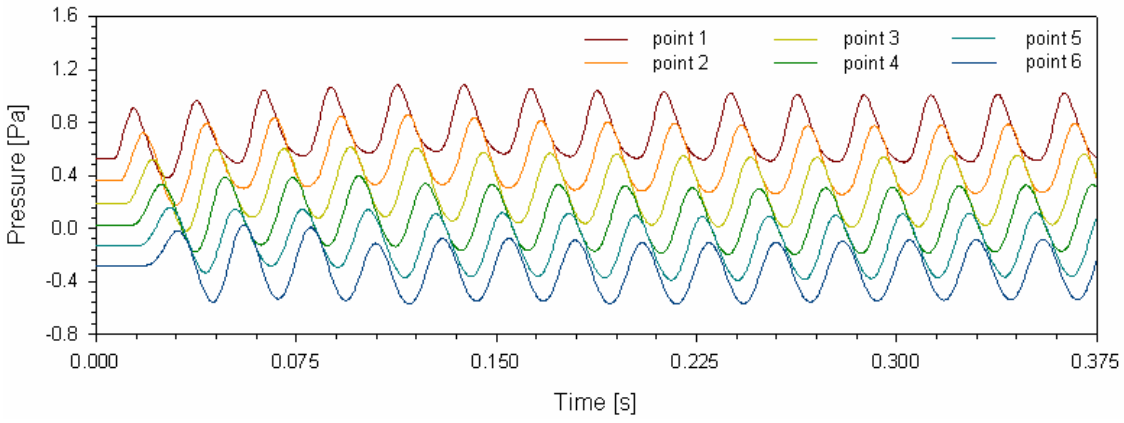

(b)

Figure 15: Convergence check for the base case of ε=0.75 with the grid size of 20 × 40 per unit cell for (a) velocity and (b) pressure

Table 2: Mass conservation check: percent differences of cycle-averaged velocities between inlet and outlet

ε	% difference at $\mathrm{Re}_{m,L}$=0.11	% difference at $\mathrm{Re}_{m,L}$=560
0.64	0.16	1.70
0.6975	0.10	1.25
0.75	0.15	0.95
0.7975	0.20	0.83
0.84	0.16	0.50

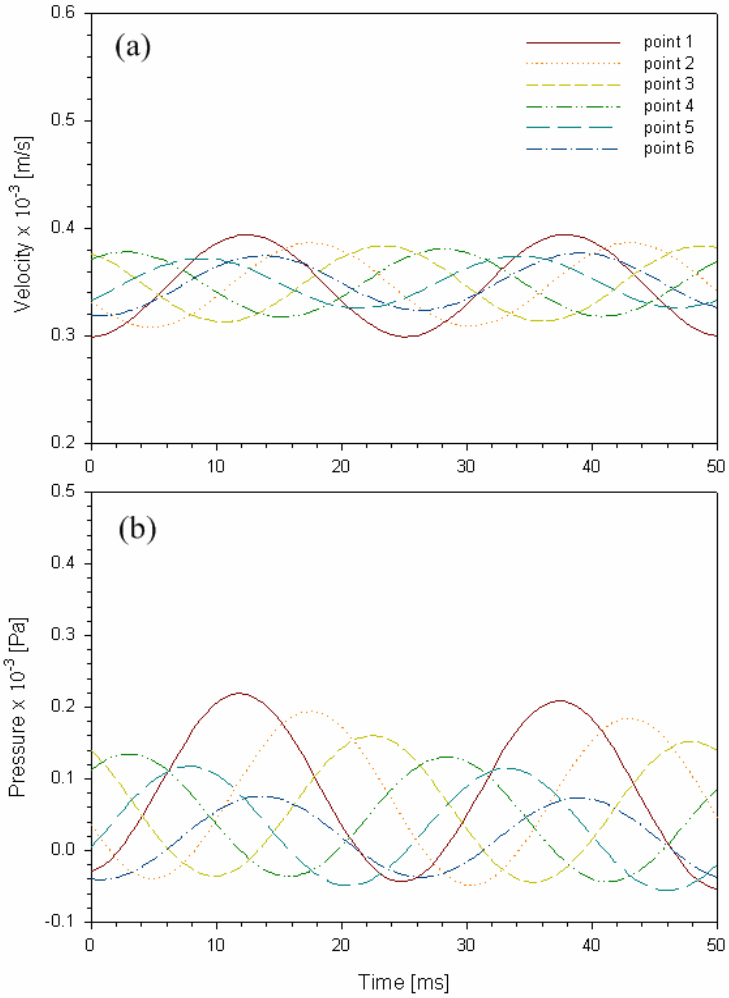

Figure 16: Variation of the instantaneous (a) velocity, and (b) pressure waves along the flow direction for the pulsating low Reynolds number flow and $\varepsilon = 0.84$

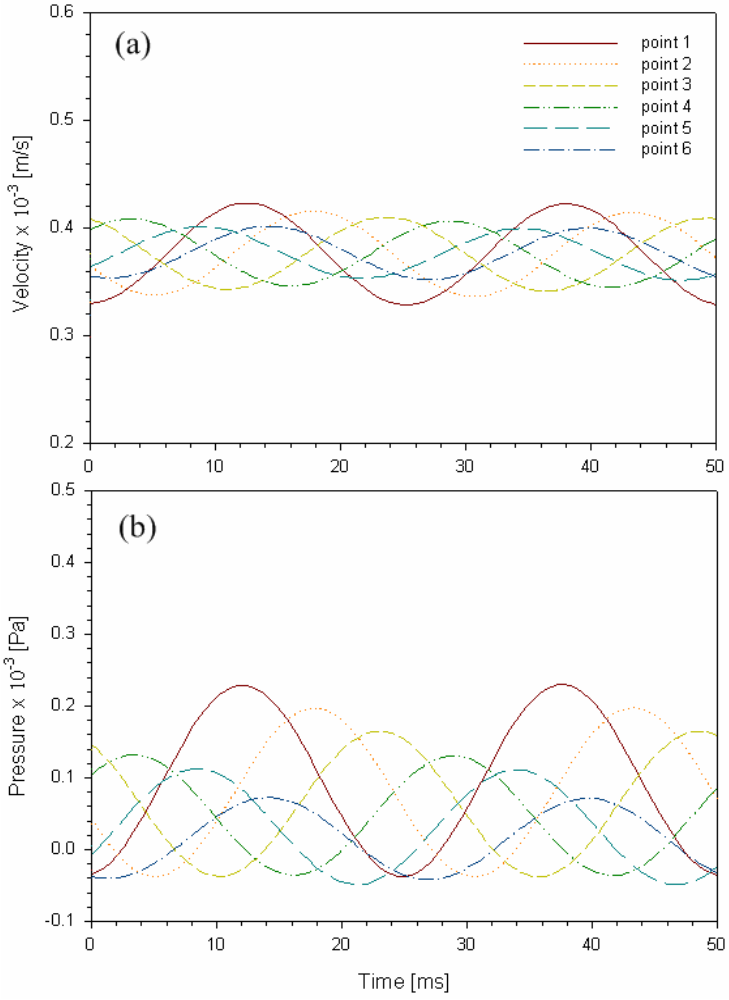

Figure 17: Variation of the instantaneous (a) velocity, and (b) pressure waves along the flow direction for the pulsating low Reynolds number flow and $\varepsilon = 0.7975$

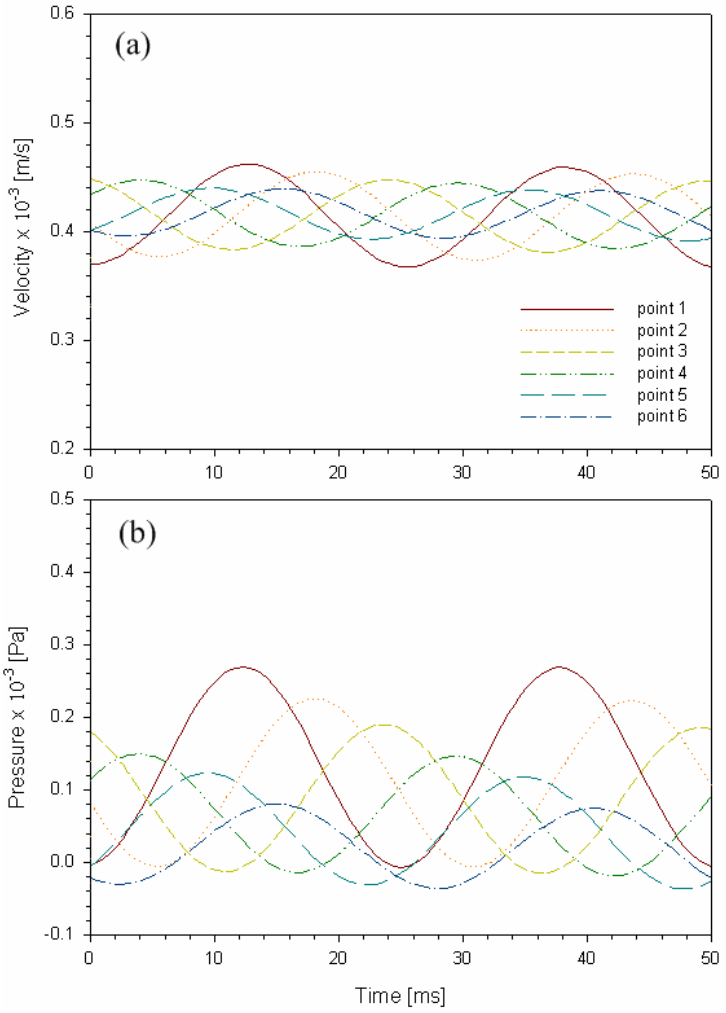

Figure 18: Variation of the instantaneous (a) velocity, and (b) pressure waves along the flow direction for the pulsating low Reynolds number flow and $\varepsilon = 0.75$

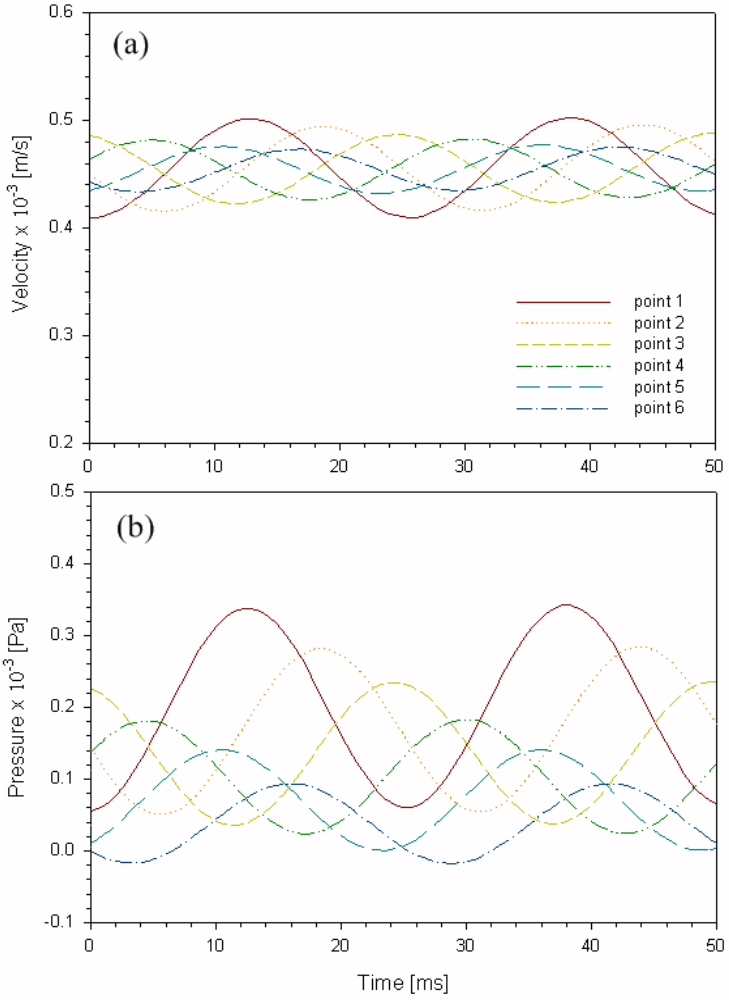

Figure 19: Variation of the instantaneous (a) velocity, and (b) pressure waves along the flow direction for the pulsating low Reynolds number flow and $\varepsilon = 0.6975$

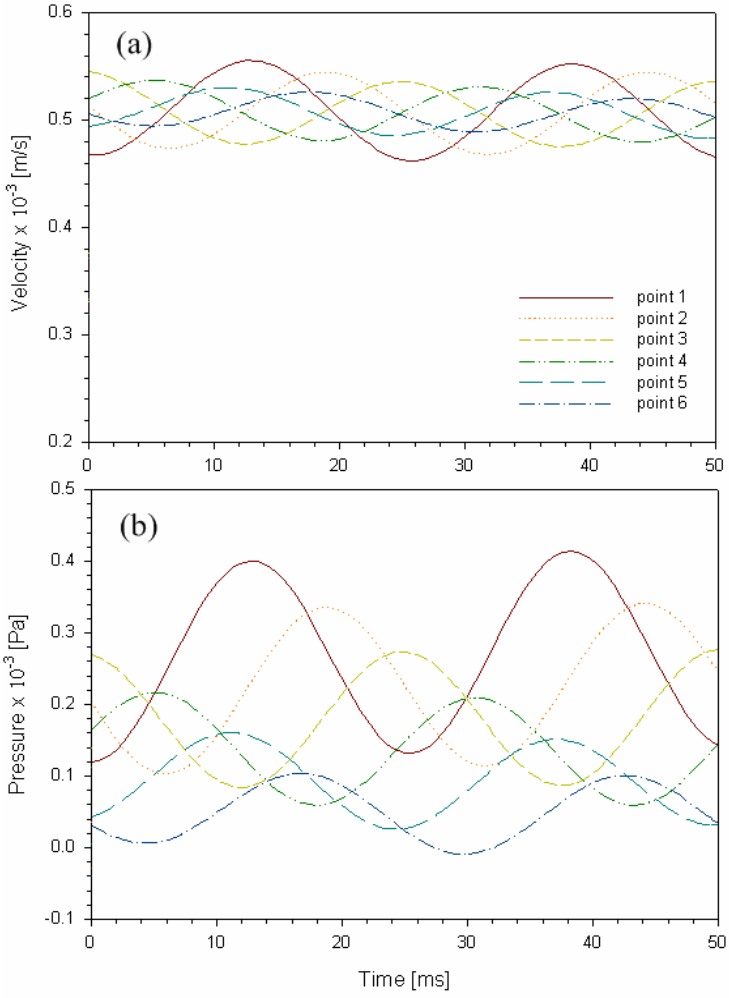

Figure 20: Variation of the instantaneous (a) velocity, and (b) pressure waves along the flow direction for the pulsating low Reynolds number flow and $\varepsilon = 0.64$

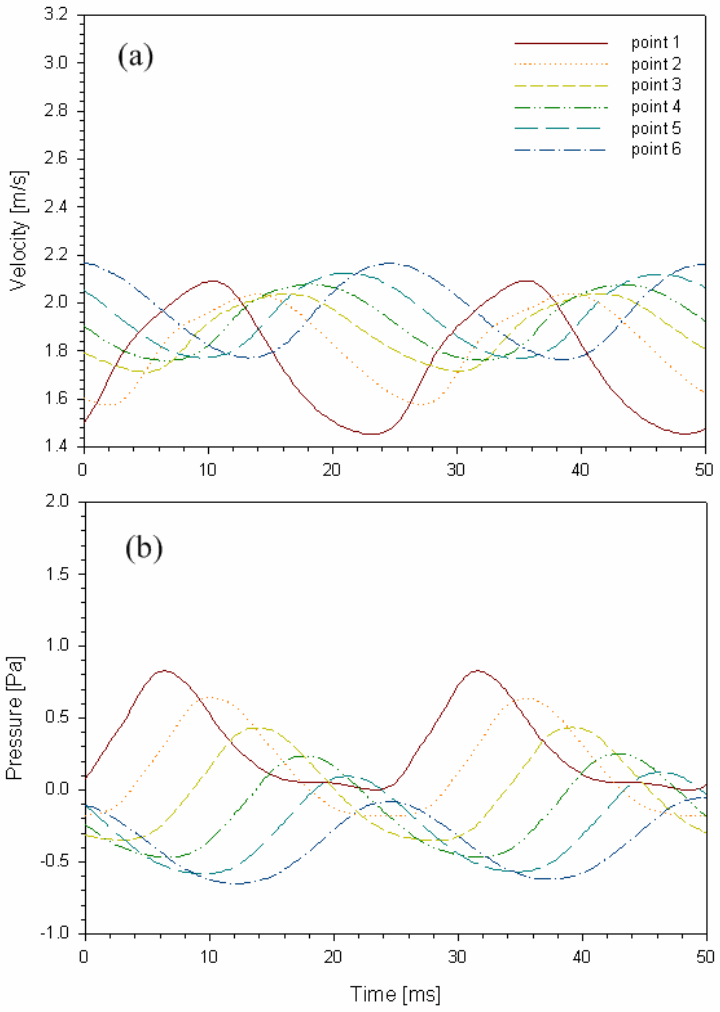

Figure 21: Variation of the instantaneous (a) velocity, and (b) pressure waves along the flow direction for the pulsating high Reynolds number flow and $\varepsilon = 0.84$

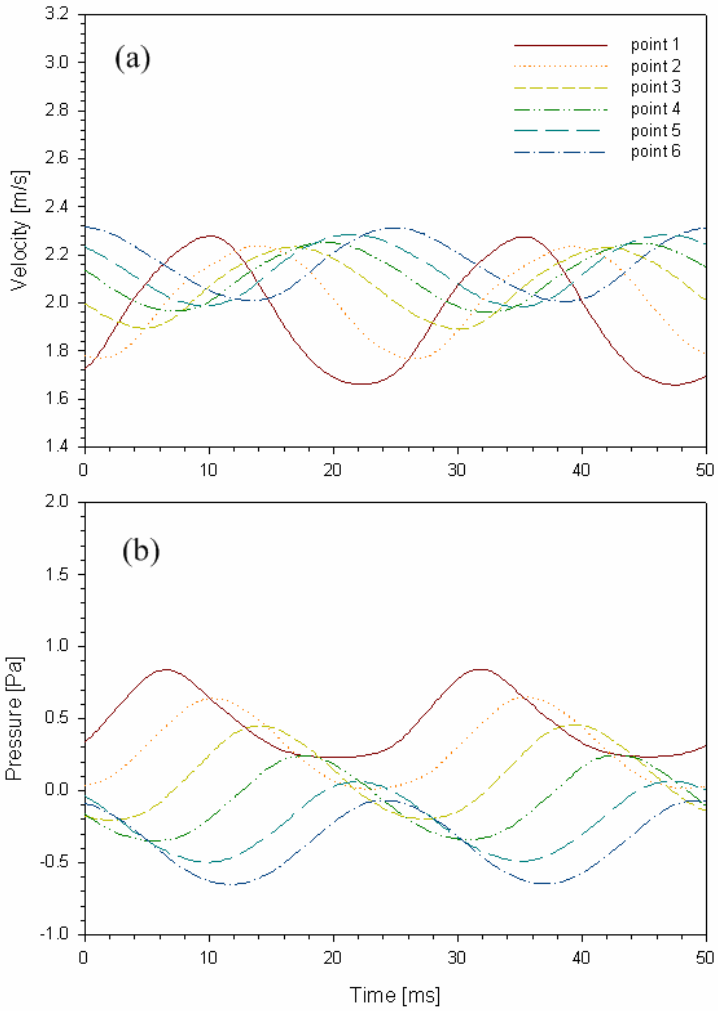

Figure 22: Variation of the instantaneous (a) velocity, and (b) pressure waves along the flow direction for the pulsating high Reynolds number flow and $\varepsilon = 0.7975$

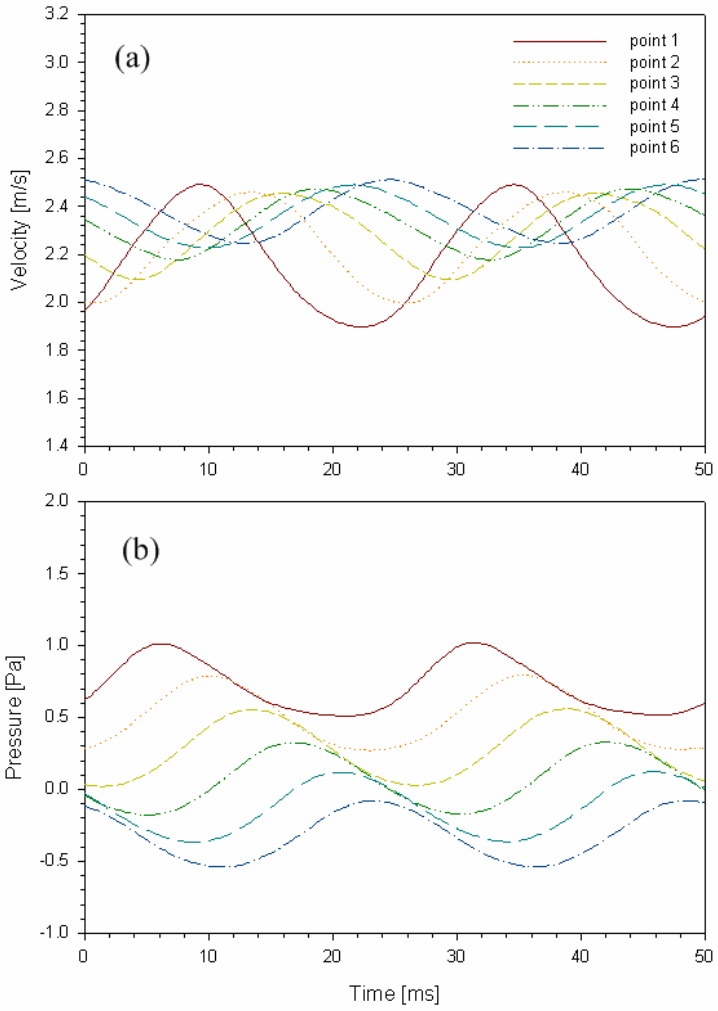

Figure 23: Variation of the instantaneous (a) velocity, and (b) pressure waves along the flow direction for the pulsating high Reynolds number flow and $\varepsilon = 0.75$

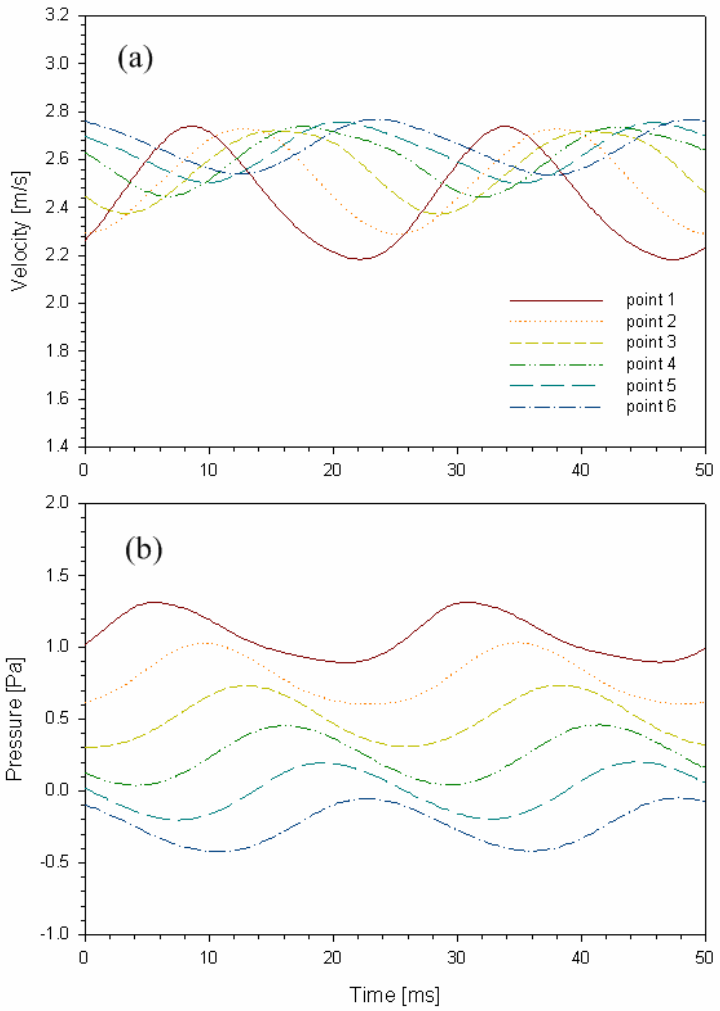

Figure 24: Variation of the instantaneous (a) velocity, and (b) pressure waves along the flow direction for the pulsating high Reynolds number flow and $\varepsilon = 0.6975$

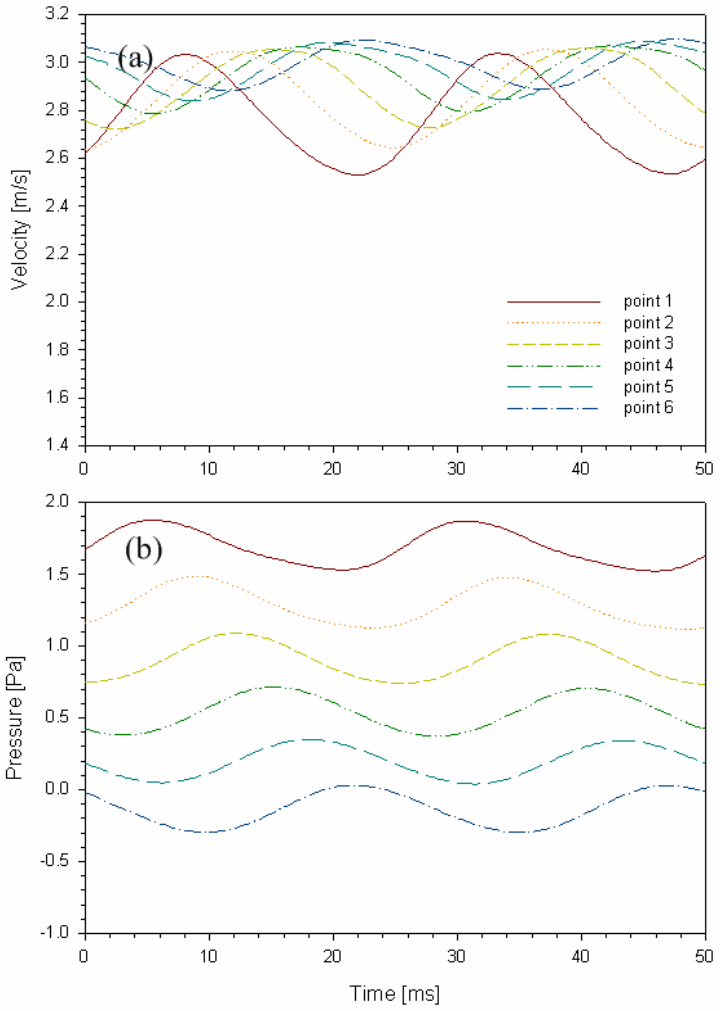

Figure 25: Variation of the instantaneous (a) velocity, and (b) pressure waves along the flow direction for pulsating high Reynolds number flow and $\varepsilon = 0.64$

As mentioned before, with the selected grid size of 20×40 per unit cell and a time step size of $1.25 \times 10^{-4}\,s$ (T/200), where the period of oscillation T is 0.025 *s*, the pulsating flow calculation up to 0.375 *s* of total time are continued until the values of instantaneous velocities and pressures at Points 1 to 6 reach the cyclic steady state condition. Figures 16-20 represent the instantaneous velocities and pressures along the flow direction during the last two cycles of pulsation (0.005 *s*) based on the mean Reynolds number $\mathrm{Re}_{m,L}$ =0.11. Figures 21-25 show similar results for $\mathrm{Re}_{m,L}$ =560. Although the pulsating inlet velocity is sinusoidal, the calculated velocity and pressure waves are not exactly sinusoidal, as shown in Figures 16-25. It should be noted that the amplitudes of instantaneous velocity and pressure waves are attenuated along the flow direction, and that there exists a considerable phase shift between instantaneous velocity and pressure waves. The cycle-averaged instantaneous velocities at measured points increase as the porosity decreases, since the free flow cross-sectional area of a unit cell $(H - D)/2$ is reduced with decreasing porosity. When the porosity decreases, the differences of cycle-averaged instantaneous pressures between adjacent two unit cells along the flow direction are increased due to the rising flow friction. For the pulsating low Reynolds number flow, there are no significant differences among the amplitudes of instantaneous pressure waves at the unit cell center points, whereas for high Re, the instantaneous pressure waves are flattened with decreasing porosity.

Figures 26 and 27 represent the phase shifts $\Delta\theta_V$, $\Delta\theta_P$ and $\Delta\theta_{VP}$ as functions of porosity for pulsating flows. The phase shift of instantaneous velocity (pressure) for a unit cell, $\Delta\theta_V$ ($\Delta\theta_P$), is determined by averaging the phase differences between Point 1 and Point 6 representing the maximum values of the instantaneous velocity (pressure), namely

$\Delta\theta_V = (\theta_{V,pt6} - \theta_{V,pt1})/5$ and $\Delta\theta_P = (\theta_{P,pt6} - \theta_{P,pt1})/5$. Since the values of the phase shift between instantaneous velocity and pressure at Point 1 and Point 6 are different, the phase shift $\Delta\theta_{VP}$ is defined according to: $\Delta\theta_{VP} = (\Delta\theta_{VP,pt1} + \Delta\theta_{VP,pt6})/2$. For pulsating low Reynolds number flow, the values of the phase shifts $\Delta\theta_V$ and $\Delta\theta_P$ are about the same and decrease gradually with increasing porosity. However, for pulsating high Reynolds number flow, $\Delta\theta_P$ increases with increasing porosity, and the phase shifts $\Delta\theta_V$ and $\Delta\theta_{VP}$ have their maximum values at ε=0.75 and ε=0.6975, respectively. The phase shifts $\Delta\theta_V$ and $\Delta\theta_P$ for low Re are about two times larger than those for high Re, whereas the phase shifts $\Delta\theta_{VP}$ for high Re are about six times larger than those for low Re.

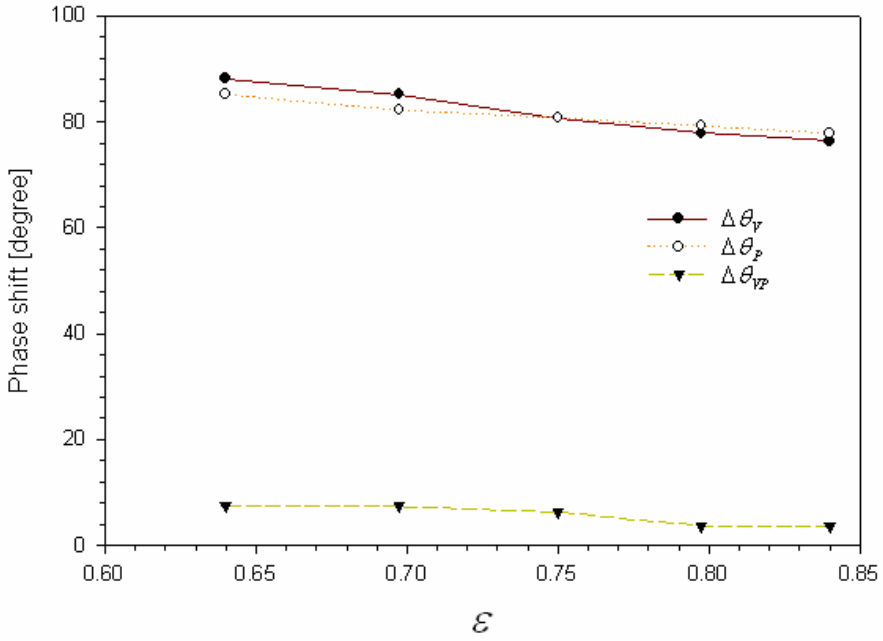

Figure 26: Phase shifts $\Delta\theta_V$, $\Delta\theta_P$ and $\Delta\theta_{VP}$ in terms of porosities for pulsating low Reynolds number flow

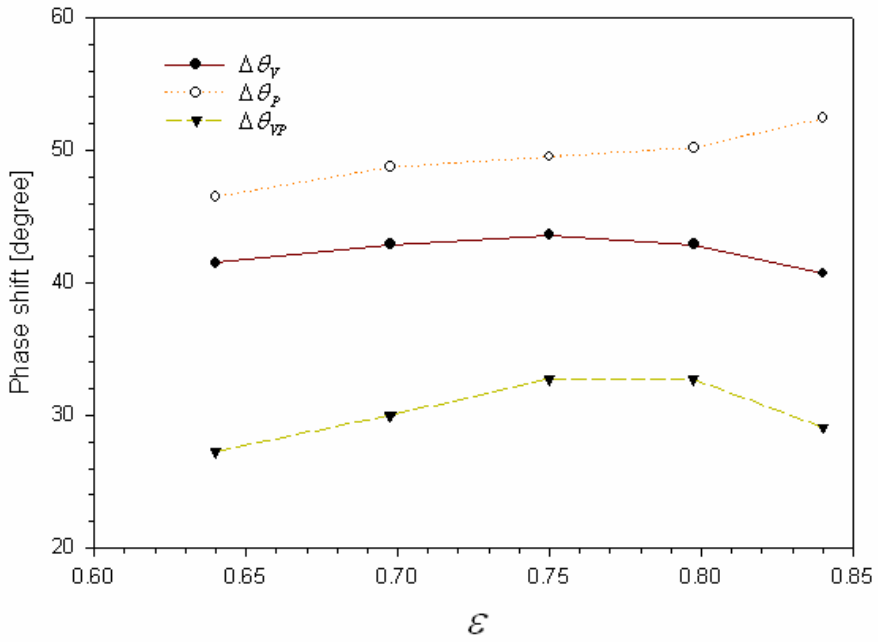

Figure 27: Phase shifts $\Delta\theta_V$, $\Delta\theta_P$ and $\Delta\theta_{VP}$ in terms of porosities for pulsating high Reynolds number flow

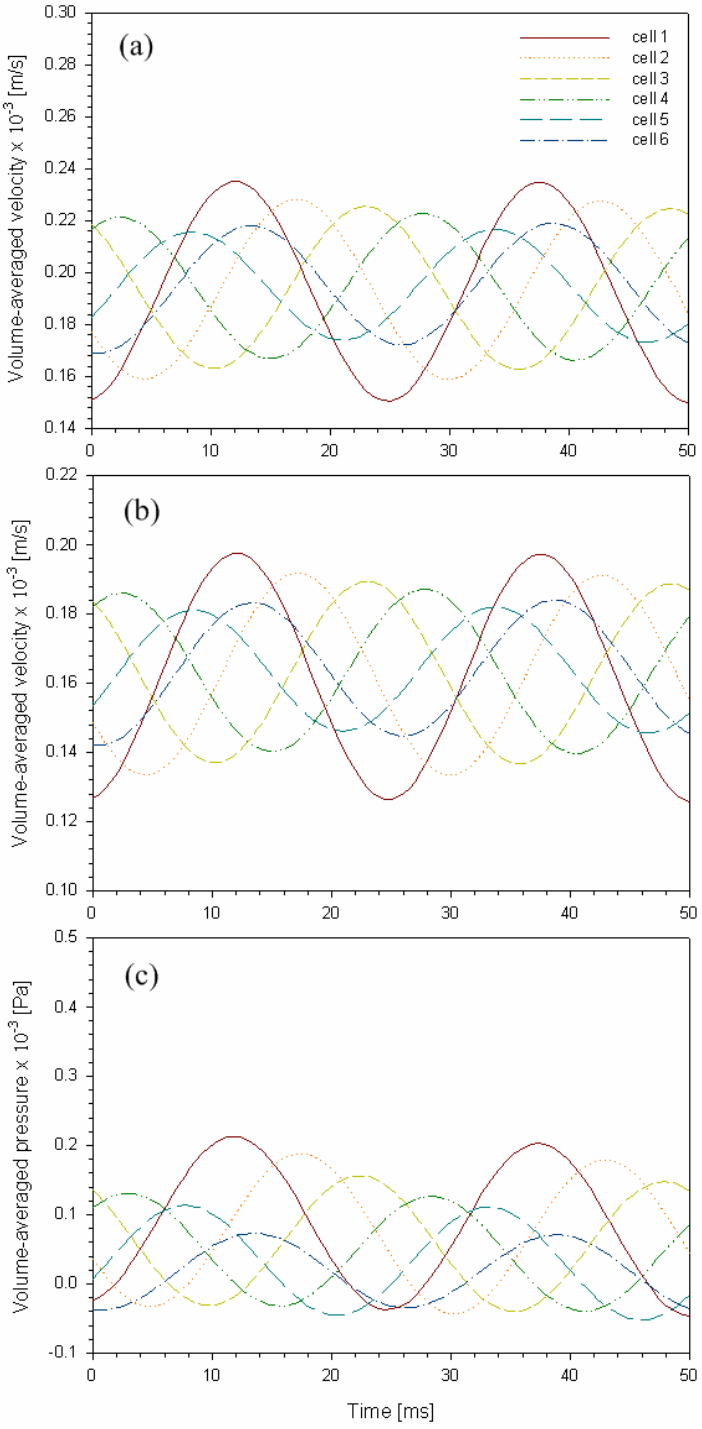

Figure 28: Variation of the volume-averaged (a) intrinsic velocity, (b) Darcy velocity, and (c) intrinsic pressure along the flow direction for the pulsating low Reynolds number flow and $\varepsilon = 0.84$

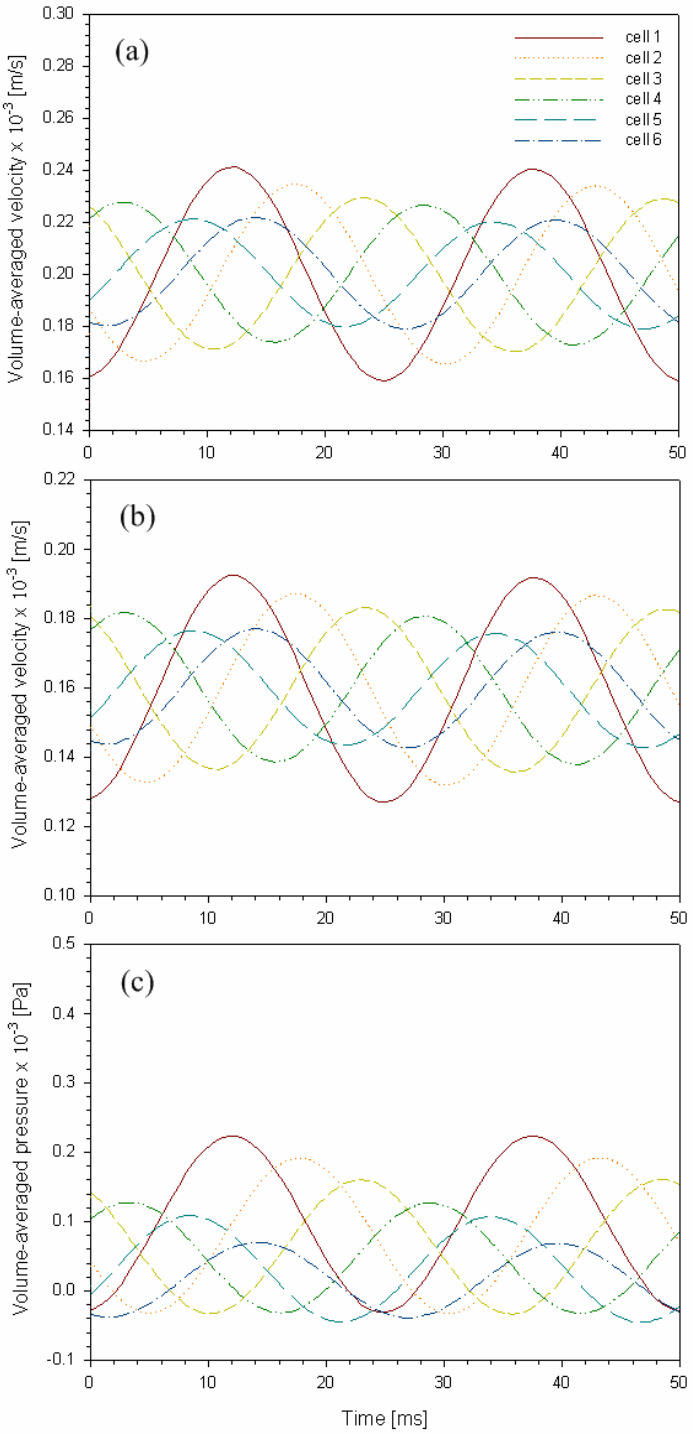

Figure 29: Variation of the volume-averaged (a) intrinsic velocity, (b) Darcy velocity, and (c) intrinsic pressure along the flow direction for the pulsating low Reynolds number flow and $\varepsilon = 0.7975$

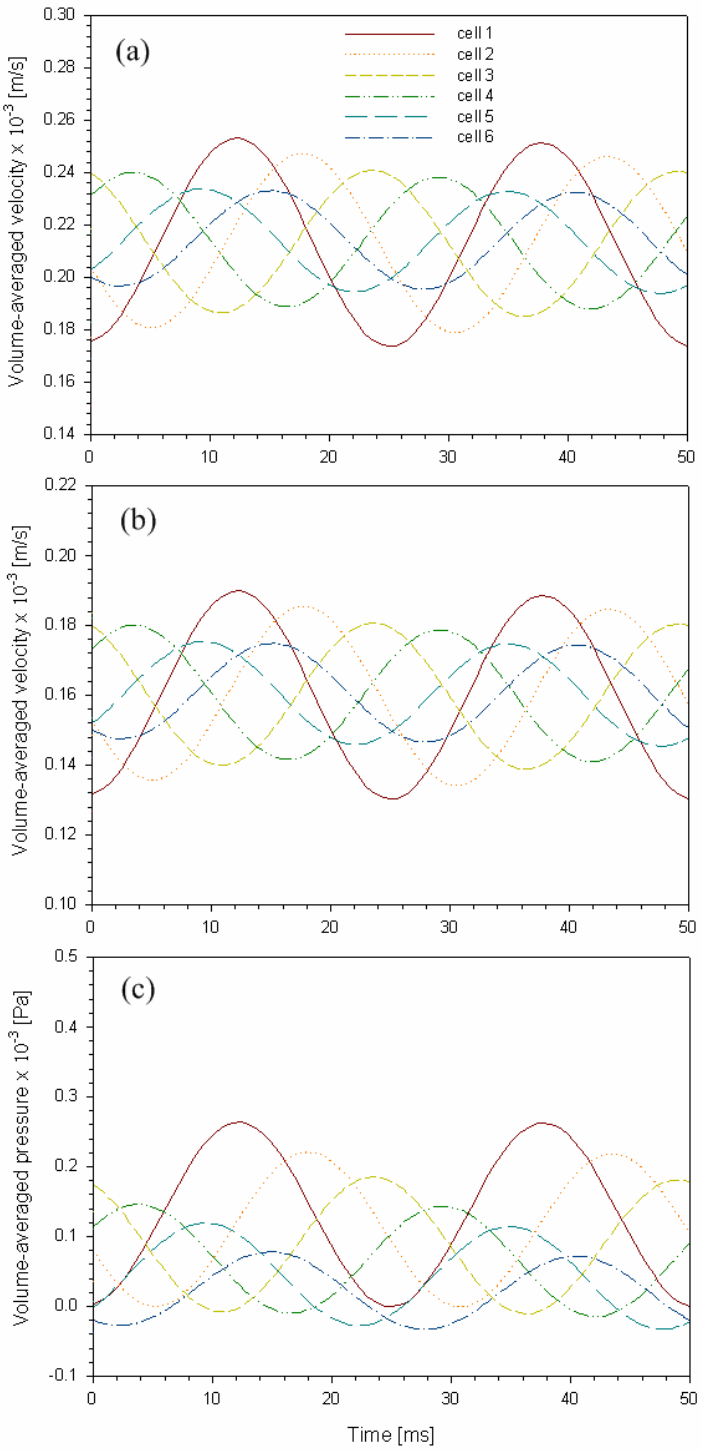

Figure 30: Variation of the volume-averaged (a) intrinsic velocity, (b) Darcy velocity, and (c) intrinsic pressure along the flow direction for the pulsating low Reynolds number flow and $\varepsilon = 0.75$

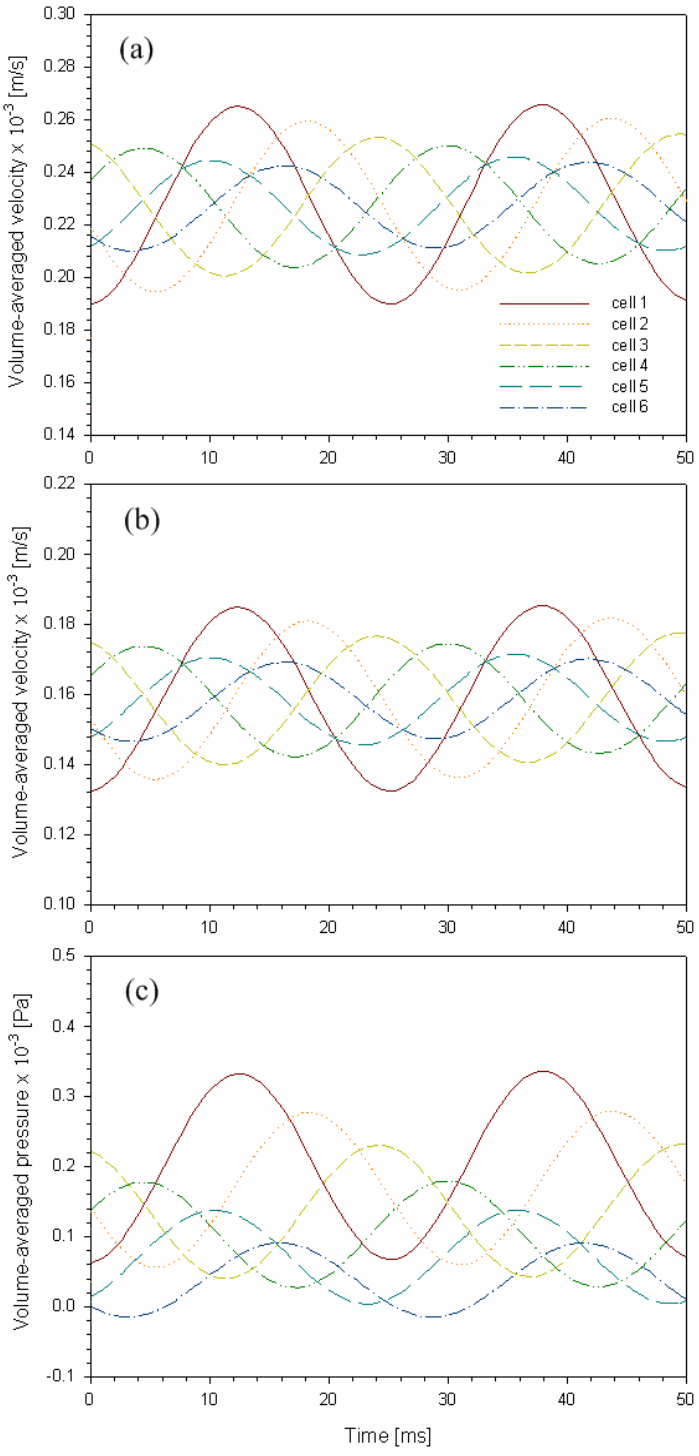

Figure 31: Variation of the volume-averaged (a) intrinsic velocity, (b) Darcy velocity, and (c) intrinsic pressure along the flow direction for the pulsating low Reynolds number flow and $\varepsilon = 0.6975$

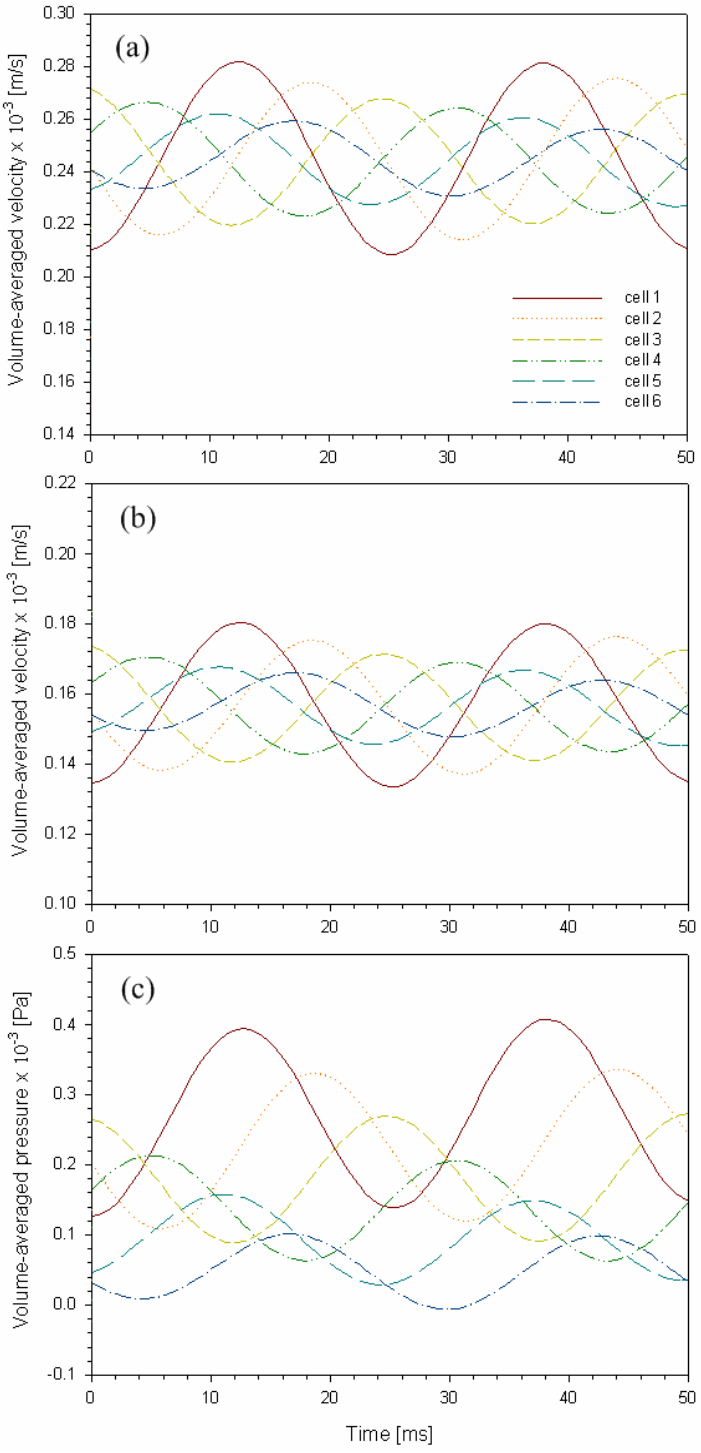

Figure 32: Variation of the volume-averaged (a) intrinsic velocity, (b) Darcy velocity, and (c) intrinsic pressure along the flow direction for the pulsating low Reynolds number flow and $\varepsilon = 0.64$

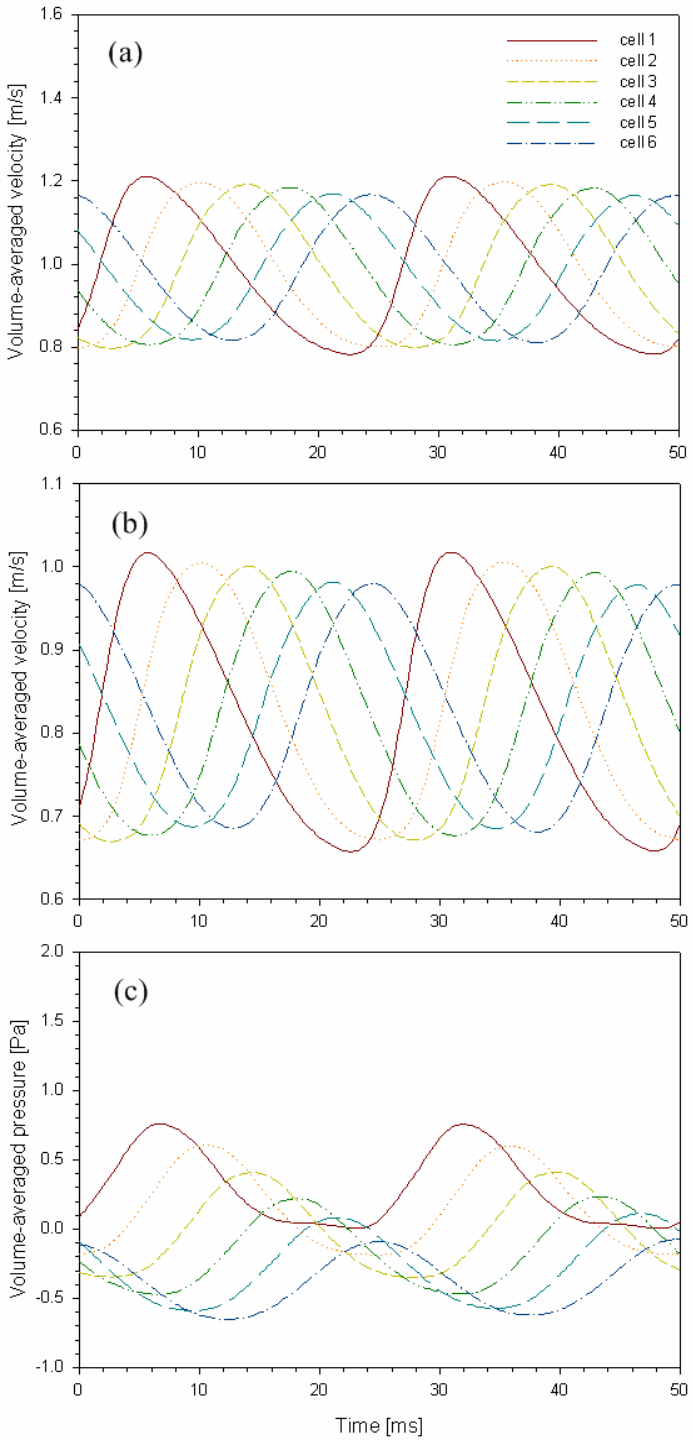

Figure 33: Variation of the volume-averaged (a) intrinsic velocity, (b) Darcy velocity, and (c) intrinsic pressure along the flow direction for the pulsating high Reynolds number flow and $\varepsilon = 0.84$

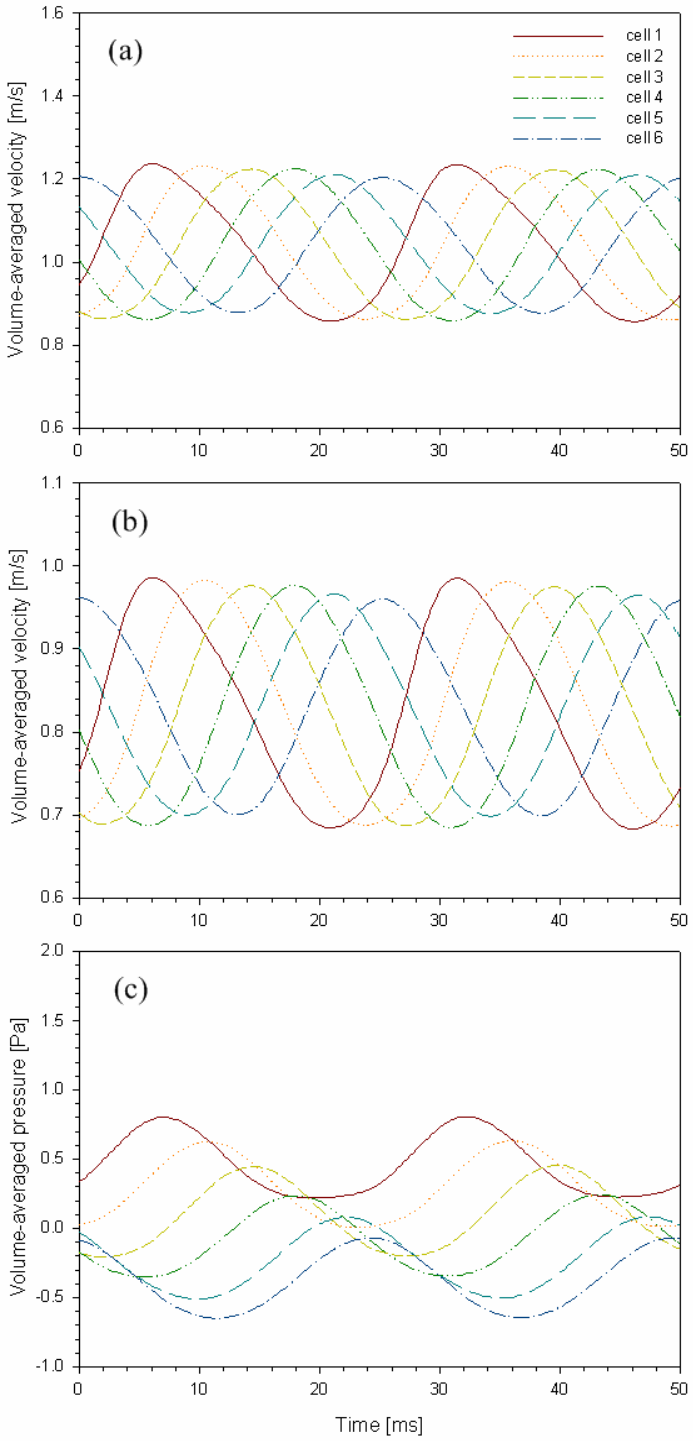

Figure 34: Variation of the volume-averaged (a) intrinsic velocity, (b) Darcy velocity, and (c) intrinsic pressure along the flow direction for the pulsating high Reynolds number flow and $\varepsilon = 0.7975$

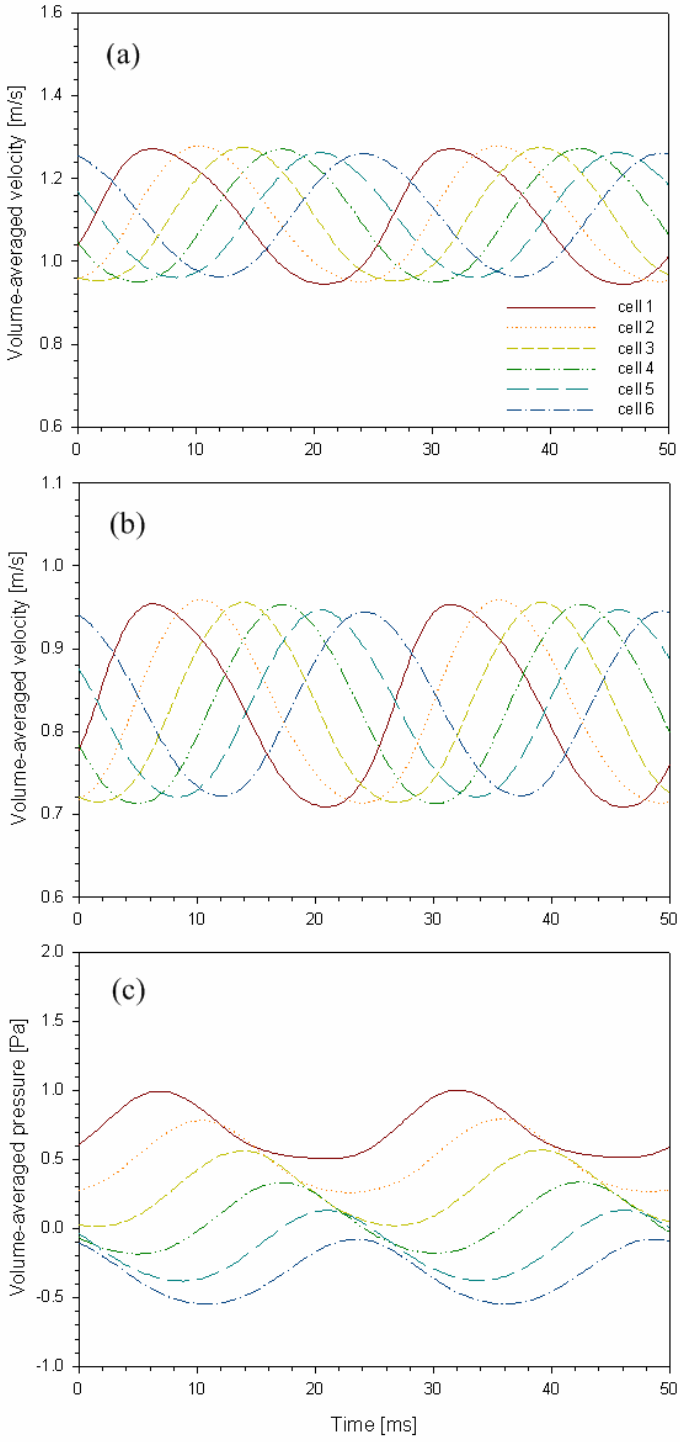

Figure 35: Variation of the volume-averaged (a) intrinsic velocity, (b) Darcy velocity, and (c) intrinsic pressure along the flow direction for the pulsating high Reynolds number flow and $\varepsilon = 0.75$

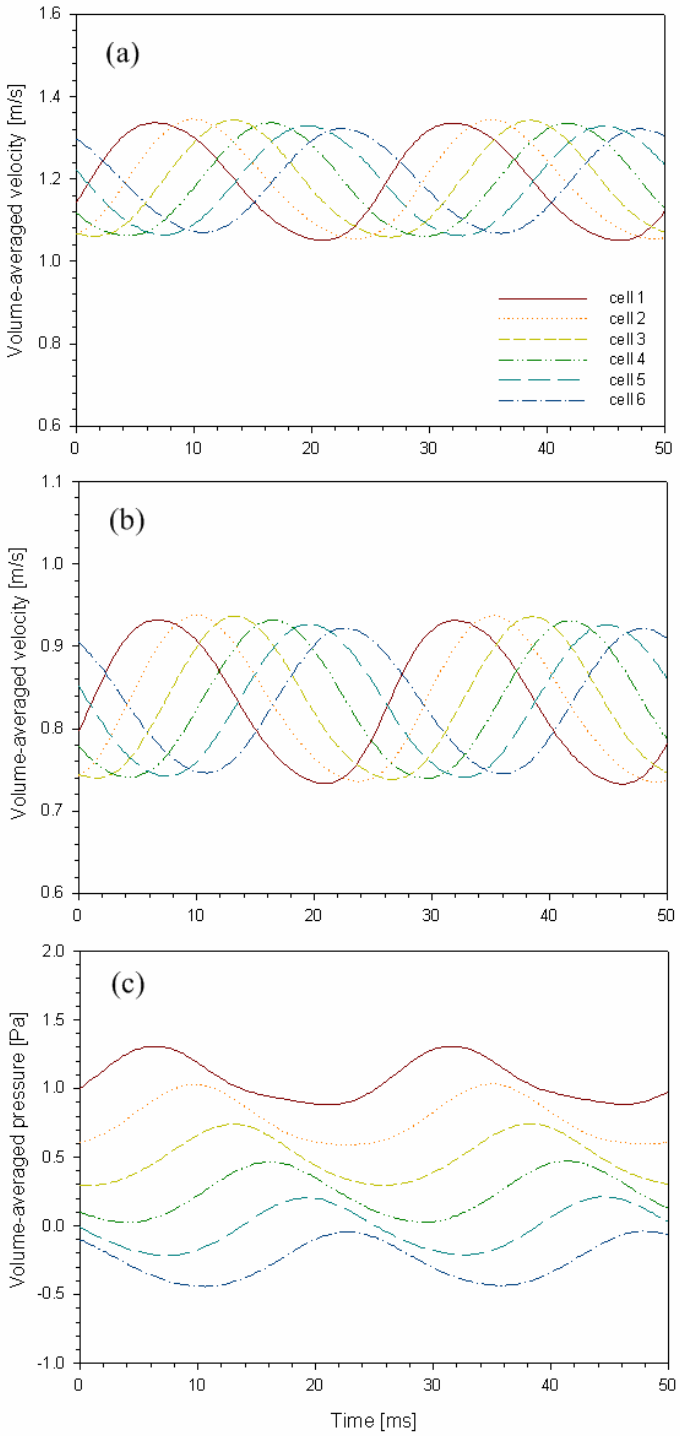

Figure 36: Variation of the volume-averaged (a) intrinsic velocity, (b) Darcy velocity, and (c) intrinsic pressure along the flow direction for the pulsating high Reynolds number flow and $\varepsilon = 0.6975$

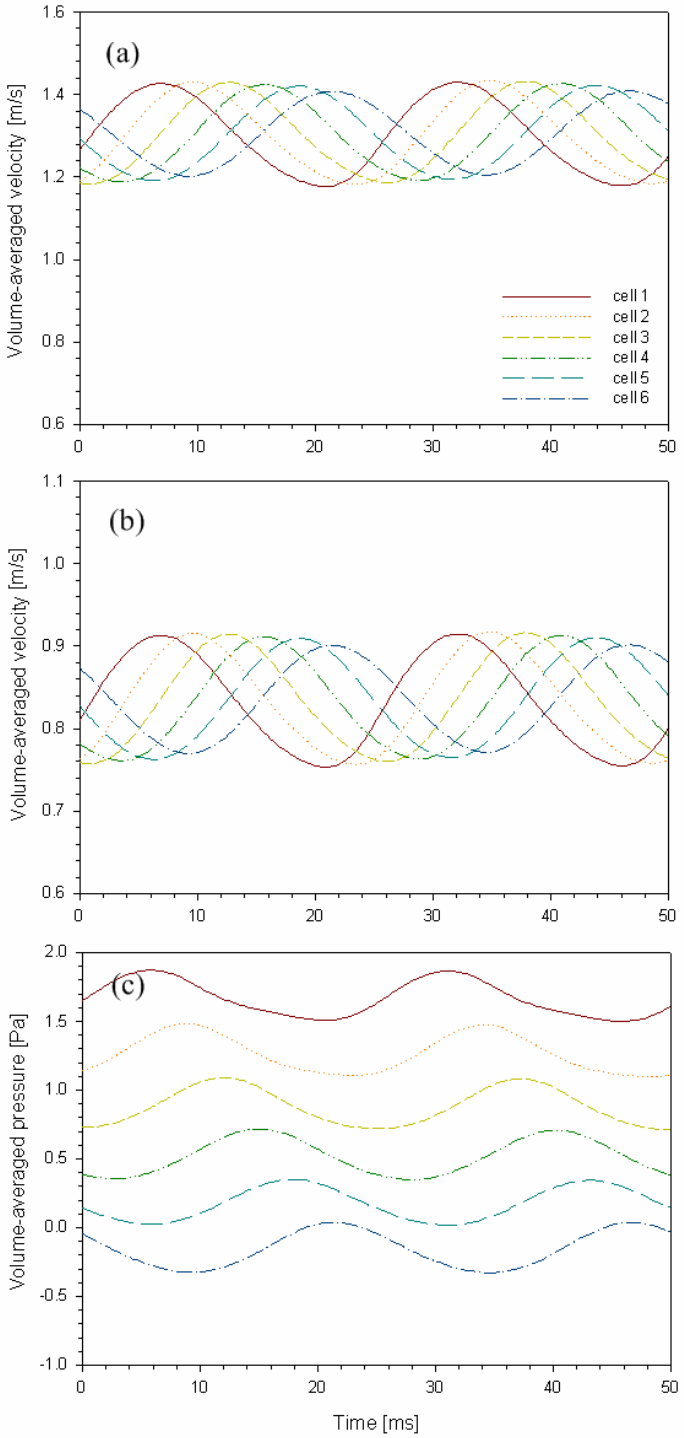

Figure 37: Variation of the volume-averaged (a) intrinsic velocity, (b) Darcy velocity, and (c) intrinsic pressure along the flow direction for the pulsating high Reynolds number flow and $\varepsilon = 0.64$

Figures 28-32 represent the instantaneous volume-averaged velocities and pressures at the unit cell centers during the last two cycles of pulsation (0.005 s) based on the mean Reynolds number $Re_{m,L}$ =0.11. Figures 33-37 display similar results for $Re_{m,L}$ =560. As mentioned before, the instantaneous volume-averaged velocities and pressures at each unit cell center of the generic porous structures are obtained by a user defined function (UDF) coded in the C^{++} programming language. Similar to the instantaneous velocity and pressure waves displayed earlier in Figures 16-25, distinct phase differences between instantaneous volume-averaged velocities and pressures can be seen in Figures 28-37. The instantaneous volume-averaged velocities and pressures are also flattened with decreasing porosity.

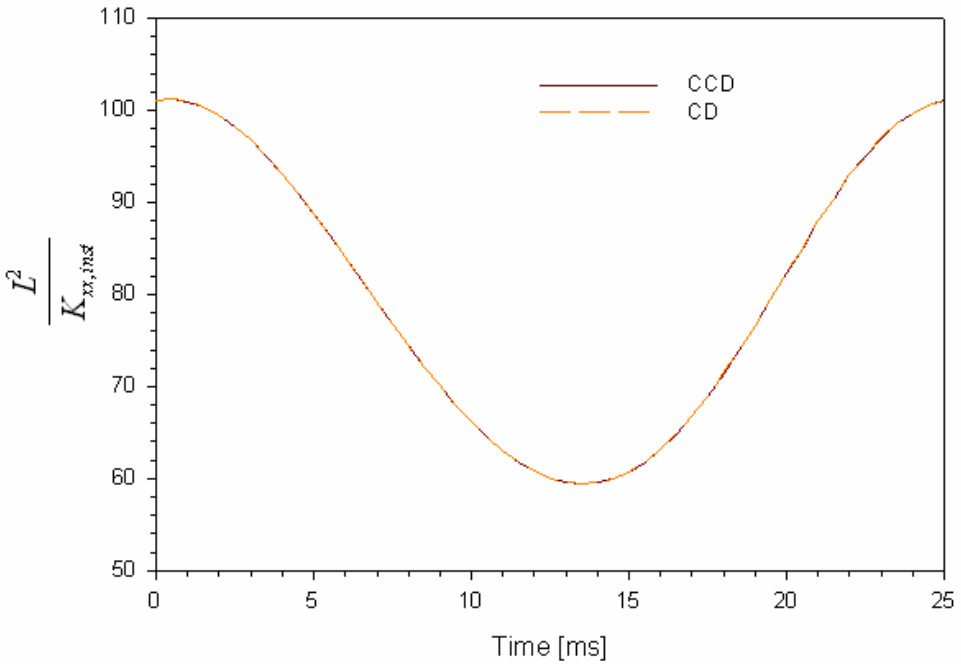

Figure 38: Variation of the instantaneous permeability coefficients due to different spatial discretization schemes for convection term

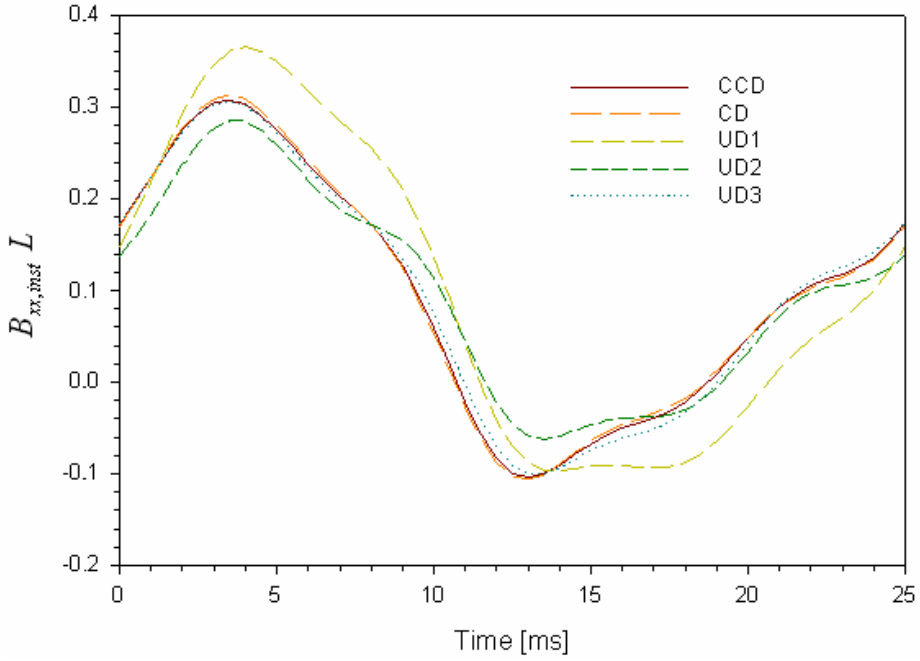

Figure 39: Variation of the instantaneous Forchheimer coefficients due to different spatial discretization schemes for convection term

In order to obtain the instantaneous permeability and Forchheimer coefficients, the unsteady volume-averaged momentum equations are solved numerically using the finite difference method, as discussed earlier in Section 2.4. For the discretization of convection term of Equation (18), the effect of various numerical schemes is examined. In case of low-flow simulations, second-order conservative (CCD) and nonconservative (CD) central difference schemes are employed to the convection term of Equation (18), and the instantaneous permeability of CCD scheme is the same as that for CD scheme (see Figure 38). For high-flow simulation, upwind discretization schemes (UD1, UD2 and UD3) for convection term are examined in addition to central difference schemes (CCD and CD). As shown in Figure 39, first-order upwind scheme (UD1) is more diffusive and less accurate than UD2 and UD3 schemes, and the instantaneous Forchheimer coefficient of third-order

upwind scheme (UD3) shows nearly similar distribution to that of CCD and CD schemes. That is, a second-order nonconservative scheme (CD) for convection term has been found to be suitable and used for the following high- as well as low-flow simulations.

The Backward in Time and Central in Space (BTCS) numerical scheme is used for the solution of Equation (18). A program was coded by using the C^{++} programming language, and the instantaneous permeability and Forchheimer coefficients during the last two cycles of pulsation (0.005 *s*) were calculated based on the aforementioned microscopic flow results (See Figures 40 and 41). For instantaneous permeability coefficients, the amplitude as well as cycle-averaged value of permeability coefficient increase with decreasing porosity.

An interesting observation is that in the transient analyses dealing with pulsating flow, starting from about 10 to 20 *ms*, the values of instantaneous Forchheimer coefficient were negative, since the left hand side of the unsteady volume-averaged momentum equation, Equation (18), which presents the local and convective acceleration terms, is less than the pressure drop term in the same equation. When the porosity increases, the portion of the cycle, in which the value of instantaneous Forchheimer coefficient is negative, is extended. The reason is that the pressure drop term in the volume-averaged momentum equation decreased with increasing porosity, whereas the value of left hand side of Equation (18) only slightly varies as a result of a change of porosity, in comparison with the variation of pressure term of right hand side. The negative values for the Forchheimer coefficient is of course a result of the phase shift between the pressure and velocity waves, and will appear to be counter-intuitive without proper attention to the phase shift. It should also be emphasized that the form of the volume-averaged porous-media momentum

equation is theoretically plausible only for quasi-steady (i.e., relatively slow transient) processes [9]. For fast transients, theory would indicate that additional, higher-order terms may be needed in the equation. Inclusion of such additional higher-order terms is not feasible at this time, however, since such terms would require additional, unknown closure relations and parameters. The standard Darcy-Forchheimer volume-averaged equations are therefore generally used in the analysis of transient processes. The counter-intuitive nature of the instantaneous Forchheimer coefficients may also be considered as a reminder that instantaneous permeability and Forchheimer coefficients are of little practical value, and that attention should instead be focused on cycle-averaged coefficients.

The cycle-averaged permeability and Forchheimer coefficients calculated by using Equations (30) and (31) are shown in Figures 42 and 43. The cycle-averaged permeability coefficients were slightly larger than those for steady flow. However, the cycle-averaged Forchheimer coefficients decrease with increasing porosity, and were about two times larger than those for steady flow at the same porosity, as shown in Figure 44 and Table 3.

3.2.1 Effect of Geometric Size

The scope of this study did not include a comprehensive examination of the effect of the size scale of the simulated porous structure on the hydrodynamic and phase shift phenomena. The importance of this issue is evident, however, and this issue should be investigated in the future. A limited study was conducted, however, to examine the effect of the size scale on the phase shift phenomena, and is discussed below. The porous structure, and the simulated system, were similar to Figure 4. The physical dimensions were L=5 mm and D=2.5 mm. Two simulations were performed, one representing a

low-flow condition, the other representing a high-flow condition. In order to provide for meaningful comparison, the boundary conditions were set such that $\mathrm{Re}_{m,L}$ =0.11 (equivalent to $\mathrm{Re}_{m,P}$=0.013) for the low-flow simulation, and $\mathrm{Re}_{m,L}$=560 (equivalent to $\mathrm{Re}_{m,P}$=64.7) for the high-flow simulation.

Figures 45 and 46 display the velocity and pressure distributions, and pressure-velocity phase differences, respectively for the low-flow test. Figure 45 should be compared with Figure 18. Comparison among these figures shown that, as a result of physical size reduction, the pressure phase difference $\Delta\theta_P$ as well as pressure-velocity phase difference $\Delta\theta_{VP}$ have slightly increased. The velocity phase difference $\Delta\theta_V$ has increased only 14%.

Figures 47 and 48 depict the phase differences for the high-flow case. These should be compared with Figure 23. For this case it can be observed that, as a result of physical size reduction, the phase differences $\Delta\theta_V$, $\Delta\theta_P$ and $\Delta\theta_{VP}$ have decreased by 14, 36 and 29 percent, respectively.

The above results, although limited in scope, underscore the importance of, and need for future investigations addressing the effect of physical scale on the hydrodynamic phenomena in a comprehensive manner.

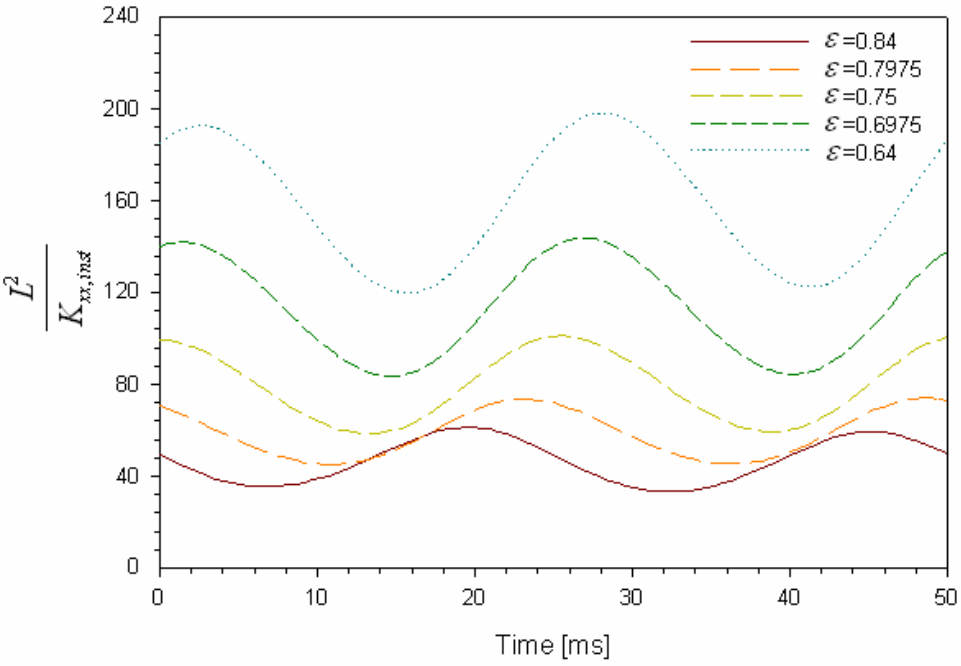

Figure 40: Variation of the instantaneous permeability coefficients for different porosities

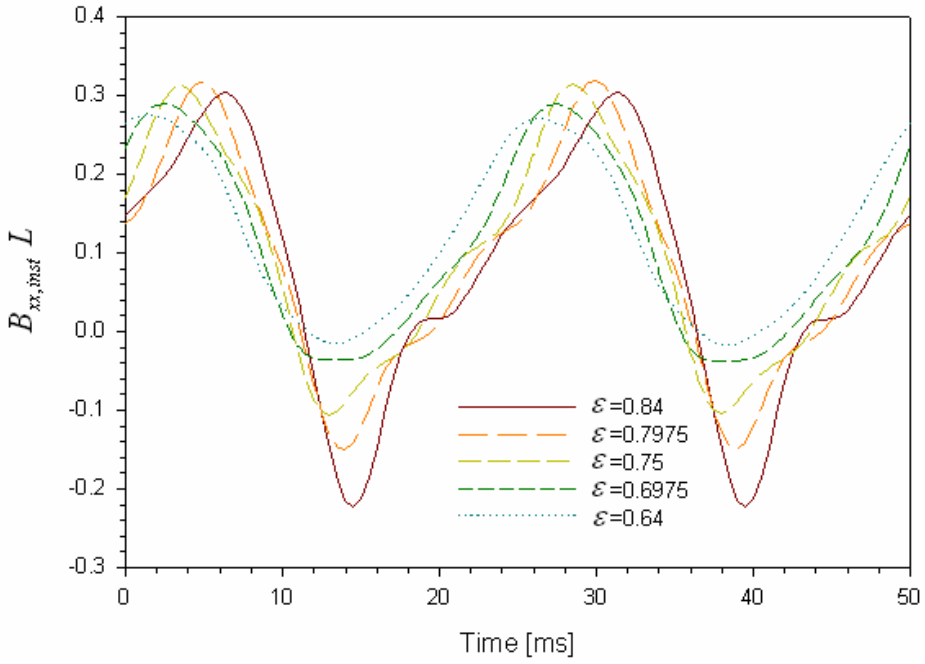

Figure 41: Variation of the instantaneous Forchheimer coefficients for different porosities

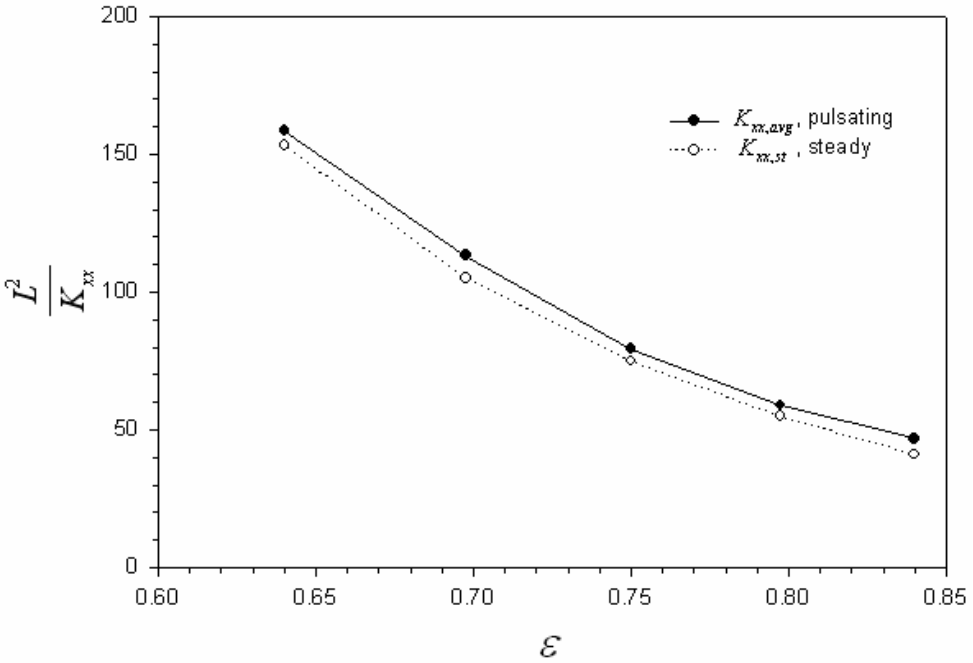

Figure 42: Comparison of the permeability coefficients between the steady and pulsating flow for different porosities

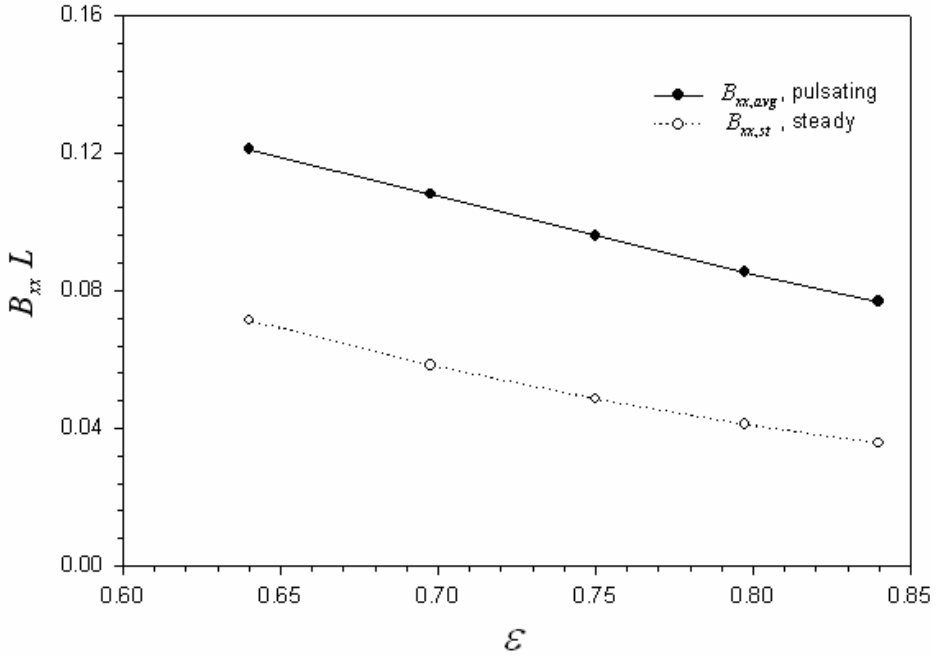

Figure 43: Comparison of the Forchheimer coefficients between the steady and pulsating flow for different porosities

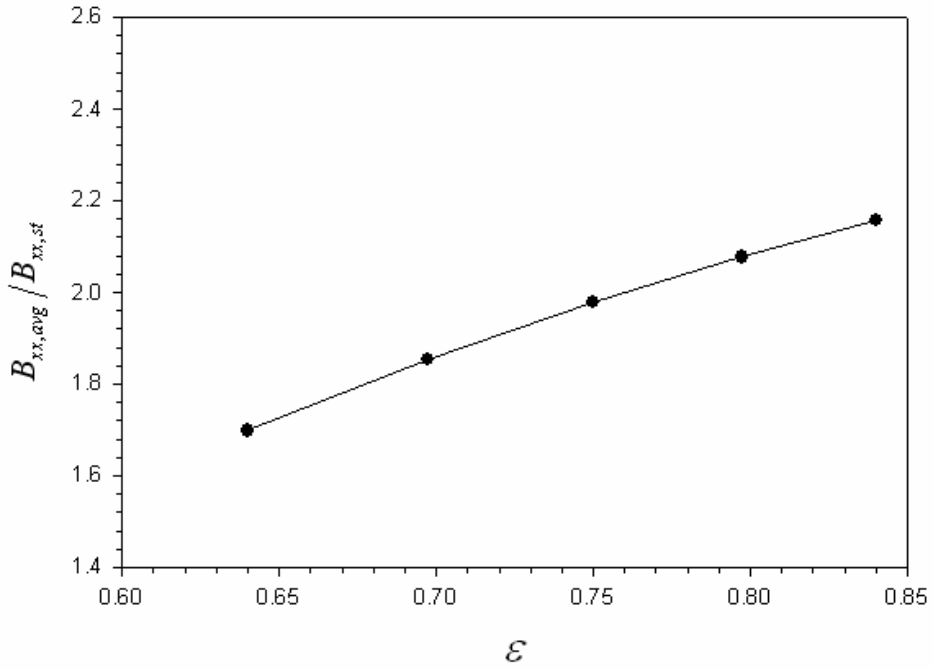

Figure 44: The Forchheimer coefficient ratio of the steady to pulsating flow for different porosities

Table 3: Comparison of permeability and Forchheimer coefficients for the steady and pulsating flows

ε	$\frac{L^2}{K_{xx,st}}$	$\frac{L^2}{K_{xx,avg}}$	$B_{xx,st}\,L$	$B_{xx,avg}\,L$
0.64	153	159	0.071	0.121
0.6975	105	113	0.058	0.108
0.75	75	79	0.049	0.096
0.7975	55	59	0.041	0.085
0.84	41	47	0.036	0.077

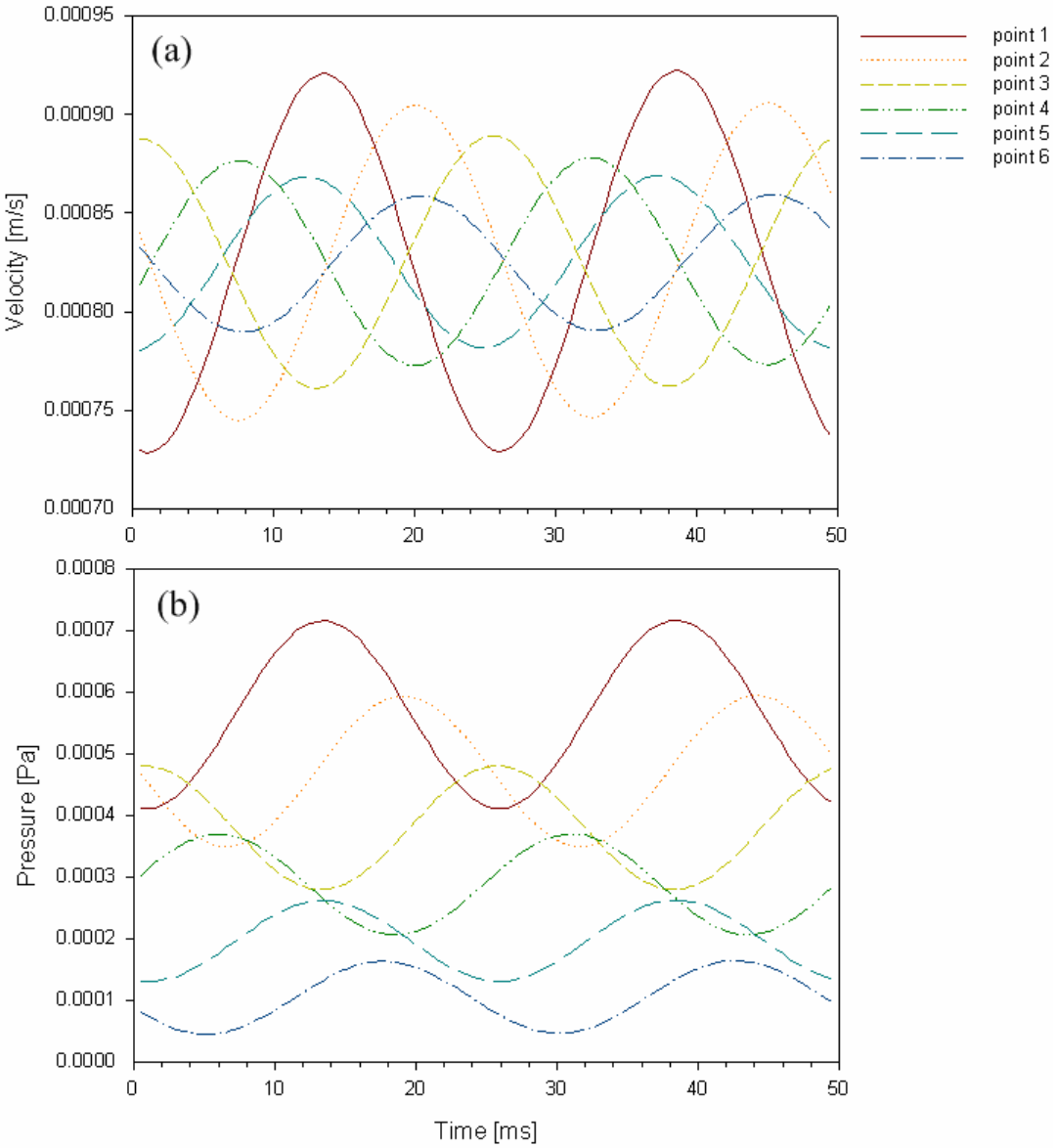

Figure 45: Variation of the instantaneous (a) velocity, and (b) pressure waves for low-flow case with $\varepsilon = 0.75$, L=5 mm, and D=2.5 mm

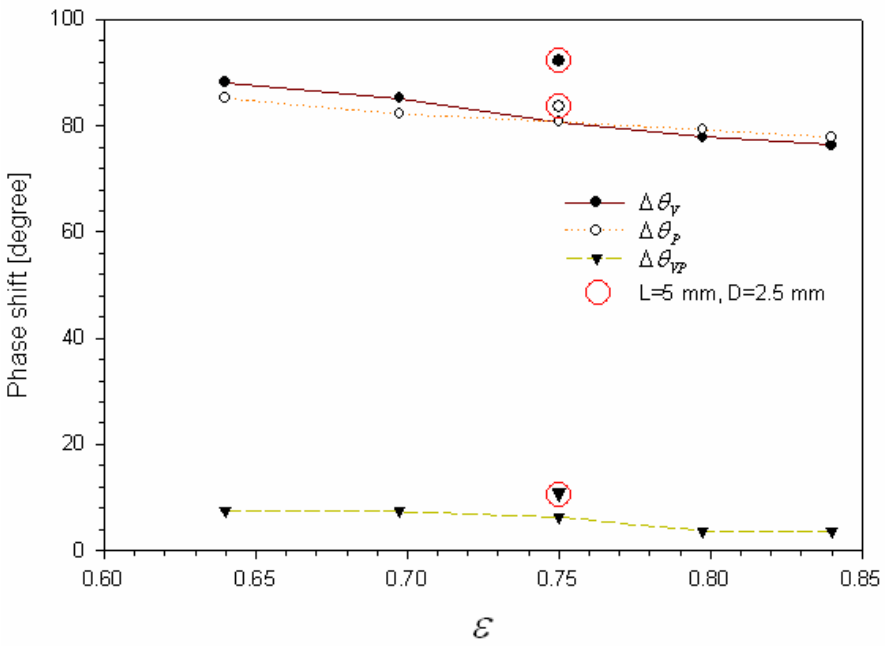

Figure 46: Comparison of phase shifts for low-flow case

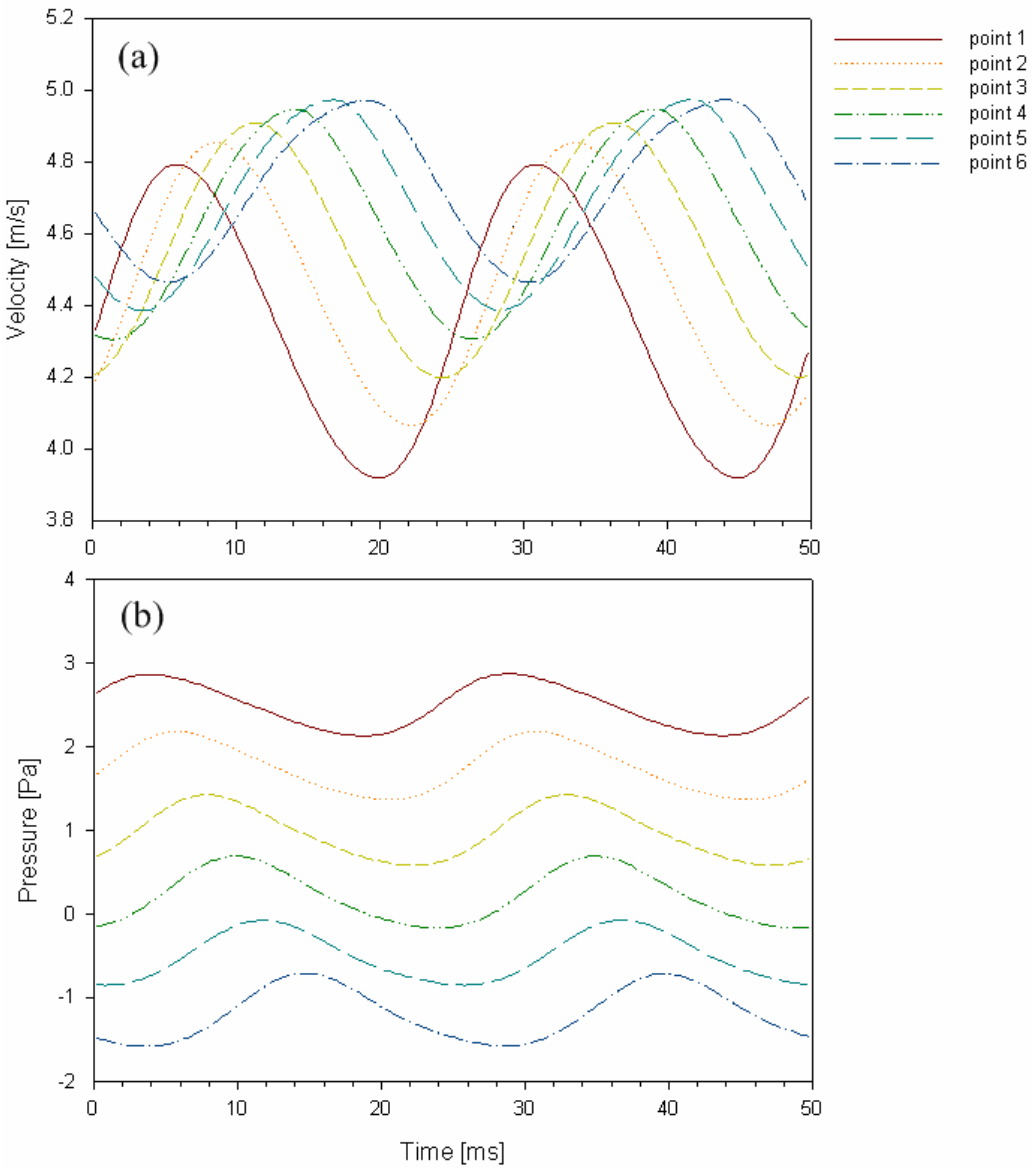

Figure 47: Variation of the instantaneous (a) velocity, and (b) pressure waves for high-flow case with $\varepsilon = 0.75$, L=5 mm, and D=2.5 mm

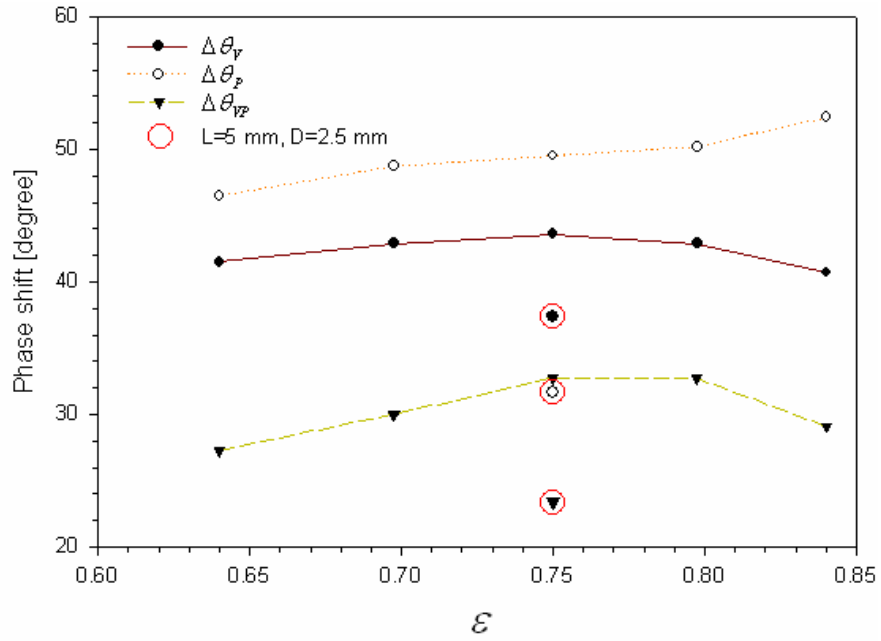

Figure 48: Comparison of phase shifts for high-flow case

CHAPTER 4

CONCLUSIONS AND RECOMMENDATIONS

4.1 Concluding Remarks

The objective of this study was to investigate, by numerical simulation, the momentum transfer parameters associated with pulsating laminar flow through porous media with a flow pulsation frequency 40 Hz. Five different generic porous structure geometries in the porosity range of 0.64 to 0.84 were generated in numerical simulations, and detailed numerical data representing the oscillating velocity and pressure variations along the flow direction were obtained by solving the microscopic governing equations. Consistent with the common practice in the literature, the generic porous structures were two-dimensional, and were formed by an array of solid rectangular-cross section rods, patterned on a rectangular pitch. The computational domain is comprised of six unit cells in series, with the first four unit cells included in order to eliminate the entrance effects. The microscopic governing equations were solved by using the CFD code FLUENT 6.3. These solutions provided the local and instantaneous velocities and pressures throughout the computational domain under steady-pulsating flow conditions. These numerical data were then utilized for the calculation of various volume-averaged properties, including the average phase shift between the adjacent unit cells with respect to velocity, pressure, and the average phase lag between velocity and pressure.

The volume-averaged velocities and pressures of each unit cell were used to numerically calculate the instantaneous as well as cycle-averaged permeability and Forchheimer coefficients for use in the volume-averaged momentum equation. For this purpose, a program was coded by using a programming language, C^{++}. This program

solves the unsteady volume-averaged momentum equation implicitly by using the finite difference method with BTCS implicit scheme which is based on a second derivative in space and first derivative in time.

The instantaneous permeability and Forchheimer coefficients were then calculated implicitly from the volume-averaged momentum equation by using the finite difference method. The results confirmed that pulsating flow through porous media leads to phase shifts in velocity and pressure. The magnitudes of the phase shifts depended on the Reynolds number. The velocity phase shifts $\Delta\theta_V$ and pressure phase shifts $\Delta\theta_P$ for low Re were about two times larger than those for high Re, whereas the phase shifts between velocity and pressure $\Delta\theta_{VP}$ for high Re were about six times larger than those for low Re. The cycle-averaged permeability coefficients were slightly larger than those for steady flow. However, the cycle-averaged Forchheimer coefficients decrease with increasing porosity, and were about two times larger than those for steady flow at the same porosity.

4.2 Recommendations for Future Work

1. Numerical simulations dealing with smaller pore sizes, representing finer porous microstructures that are used in miniature cryocoolers is recommended. In this study, the size of a square rod, *D,* that is used to construct the generalized porous medium was varied from 4 mm for ε =0.84, to 6 mm for ε =0.64. These sizes clearly do not represent the microporous structures used in modern and future miniature cryocoolers. More realistic simulations with the unit cell sizes corresponding to about D=20 μm to 60 μm are recommended for the future work.
2. Unfortunately, relevant experimental or numerical data which would verify the

accuracy of the current simulation results for pulsating flow could not be found in the literature. Such data are badly needed.

3. The potential thermal non-equilibrium between the porous structure and pulsating flow in the regenerators of cryocoolers can affect these cryocoolers' performance. Little is known about the extent of such thermal non-equilibria Therefore, in order to understand the solid-fluid heat transfer characteristics, a detailed pulsating flow simulation for a generic porous structure geometry has to be performed. Detailed numerical data representing the temperature variations for some generic porous structure geometries could be obtained from the microscopic energy conservation equation. The standard unsteady volume-averaged energy conservation equations for porous media can then applied in order to achieve solid surface-fluid heat transfer coefficients, the thermal dispersion, etc.
4. Finally, experimental verification is needed for the accuracy of the permeability, Forchheimer and solid surface-fluid heat transfer coefficients for pulsating flow that are obtained from pure simulation.

APPENDIX A

FLUENT USER DEFINED FUNCTION

```
#include "udf.h"

int iter;
int iter_x;
int iter_y;
int iter_time=0;

real u_right[1000];
real v_right[1000];
real u_top[1000];
real v_top[1000];
real u_avg_right, v_avg_right;
real u_avg_top, v_avg_top;
real p_avg_right, p_avg_left, p_avg_top, p_avg_bottom;
real ux[10][500000]; // volume-averaged x-velocity
real uy[10][500000]; // volume-averaged y-velocity
real uu[10][500000]; // volume-averaged velocity
real p[10][500000]; // volume averaged pressure
real u_center[10][500000]; // pulsating velocity at the center of unit cell
real p_center[10][500000]; // pulsating pressure at the center of unit cell

real converg_u[500000]; // check convergence of velocity
real converg_p[500000]; // check convergence of pressure
```

```
real bef_u_center=100000; // dummy value
real bef_p_center=100000; // dummy value

real y;

int right_buffer; // grid size of right buffer
int left_buffer; // grid size of left buffer
int num_unitcell; // grid size of a unit cell

//////////////////////
int num_period; // period
int num_cell;
int num_center;
int num_cell_tot; // number of cells in domain
int num_block; // number of iterative unit cell
int calc_block; // unit cell number to calculate
int num_start; // first grid number
int num_end; // final grid number
real p_avg_block; // volume-averaged pressure

real pi = 3.141592;
real uf; // intrinsic average velocity
real uf_x, uf_y;
real u;  // darcy velocity
real phi; // porosity
real rho=1.225;
real vis=0.000017894;
```

```
real ReL; // ReL=(rho*u*L)/vis

FILE *fin;
FILE *fout1, *fout2;

// Pulsating velocity profile at inlet boundary
DEFINE_PROFILE(velocity_right, thread, position)
{
  face_t f1;
  real t = CURRENT_TIME;

  real U = 0.818;
  real a = 0.4;
  real w = 2. * 3.141592 * 40.;

  begin_f_loop(f1, thread)
    {
      F_PROFILE(f1, thread, position) = U * ( 1. + a * sin(w*t) );
          }
  end_f_loop(f1, thread)
}

// get flow properties and check convergence
DEFINE_EXECUTE_AT_END(data_at_current_timestep)
{
          cell_t c, c0, c1;
          face_t f1, f2;
```

```
Thread *c_thread, *t0, *t1, *t2, *t3;
Domain *domain = Get_Domain(1);
iter_time = iter_time+1;

num_cell = 1;
thread_loop_c(c_thread, domain)
{
        begin_c_loop(c, c_thread)
        {
                num_cell = num_cell + 1;
        }
        end_c_loop(c, c_thread)
}
num_cell_tot = num_cell - 1;

for (calc_block=1; calc_block<=6; calc_block++){
        num_start = (right_buffer+left_buffer) + num_unitcell
                * (calc_block-1) + 1.;
        num_end = (right_buffer+left_buffer) + num_unitcell
                * calc_block;

        num_cell = 1;
        uf_x = 0;
        uf_y = 0;
        p_avg_block = 0;
        thread_loop_c(c_thread, domain)
        {
```

```
begin_c_loop(c, c_thread)
{
// get volume-averaged velocity and pressure
if (num_cell >= num_start && num_cell <= num_end){
        uf_x = uf_x + C_U(c,c_thread);
        uf_y = uf_y + C_V(c,c_thread);
        p_avg_block = p_avg_block + C_P(c,c_thread);

        // get pulsating velocity and pressure at the center of unit cell
        if (num_cell == num_start+num_center){
                u_center[7-calc_block][iter_time] = C_U(c,c_thread);
                p_center[7-calc_block][iter_time] = C_P(c,c_thread);

        // check convergence
                if (iter_time % num_period == 0){
                        converg_u[iter_time] =
                                (u_center[7-calc_block][iter_time]
                                -bef_u_center)/bef_u_center;
                        converg_p[iter_time] =
                                (p_center[7-calc_block][iter_time]
                                -bef_p_center)/bef_p_center;

                        bef_u_center = u_center[7-calc_block][iter_time];
                        bef_p_center = p_center[7-calc_block][iter_time];
                }
        }
        num_cell = num_cell + 1;
```

```
        }
        else{
                num_cell = num_cell + 1;
        }
        }
        end_c_loop(c, c_thread)
        }
        uf_x = uf_x / num_unitcell;
        uf_y = uf_y / num_unitcell;
        uf = sqrt (uf_x*uf_x + uf_y*uf_y);
        p_avg_block = p_avg_block / num_unitcell;

        ux[7-calc_block][iter_time] = uf_x;
        uy[7-calc_block][iter_time] = uf_y;
        uu[7-calc_block][iter_time] = uf;
        p[7-calc_block][iter_time] = p_avg_block;
}

// write data file
fout1 = fopen("11111_Results.txt", "a");
fprintf(fout1, "iter_time  ux[][]  uy[][]  uu[][]  p[][]
        u_center[][]  p_center[][]  converg_u[iter_time]  converg_p[iter_time]");
fprintf(fout1, " %d ", iter_time);

for (iter=1; iter<=6; iter++){
        fprintf(fout1, "%g ", ux[iter][iter_time]);
}
```

```
        for (iter=1; iter<=6; iter++){
                fprintf(fout1, "%g ", uy[iter][iter_time]);
        }
        for (iter=1; iter<=6; iter++){
                fprintf(fout1, "%g ", uu[iter][iter_time]);
        }
        for (iter=1; iter<=6; iter++){
                fprintf(fout1, "%g ", p[iter][iter_time]);
        }
        for (iter=1; iter<=6; iter++){
                fprintf(fout1, "%g ", u_center[iter][iter_time]);
        }
        for (iter=1; iter<=6; iter++){
                fprintf(fout1, "%g ", p_center[iter][iter_time]);
        }
        fprintf(fout1, "%g %g ", converg_u[iter_time], converg_p[iter_time]);

        fprintf(fout1, "\n");
        fclose(fout1);
}
```

APPENDIX B

C++ SOURCE CODE FOR NUMERICAL SIMULATION

```
#include <stdio.h>
#include <iostream.h>
#include <fstream.h>
#include <math.h>
#include <conio.h>
#include <iomanip.h>
#include <process.h>
#include <stdlib.h>
#include <io.h>
#include <time.h>
#include <string.h>

double vel_inlet[100000]; // flow properties for low-flow simulation
double Re[100000];
double p_1[100000];
double p_2[100000];
double p_3[100000];
double p_4[100000];
double p_5[100000];
double p_6[100000];
double u_1[100000];
double u_2[100000];
double u_3[100000];
```

```
double u_4[100000];
double u_5[100000];
double u_6[100000];

double vel_inlet_hi[100000]; // flow properties for high-flow simulation
double Re_hi[100000];
double p_1_hi[100000];
double p_2_hi[100000];
double p_3_hi[100000];
double p_4_hi[100000];
double p_5_hi[100000];
double p_6_hi[100000];
double u_1_hi[100000];
double u_2_hi[100000];
double u_3_hi[100000];
double u_4_hi[100000];
double u_5_hi[100000];
double u_6_hi[100000];

double left_term[100000]; // local + convection terms for low-flow simulation
double press_term[100000]; // pressure term for low-flow simulation
double vis_term[100000]; // viscous term for low-flow simulation
double left_term_hi[100000]; // local + convection terms for high-flow simulation
double press_term_hi[100000]; // pressure term for high-flow simulation
double vis_term_hi[100000]; // viscous term for high-flow simulation

double Kf1[100000]; // instantaneous permeability coefficients
```

```
double bf1[100000]; // instantaneous Forchheimer coefficients

main()
{
        double porosity;

        double pi = 3.141592;
        double rho, vis; // density and viscosity
        double L, H, D; // geometry

        int N;
        int dummy1;
        double dummy2;
        int iter;

        double Kf1_avg, bf1_avg; // cycle-averaged permeability
                        // and Forchheimer coefficients

        rho = 1.225;
        vis = 1.7894 * pow(10,-5);
        L = 0.01;
        H = 0.01;
        D = 0.005;
        double time_step = 0.000125; // time-step size

        porosity = (L*H - D*D) / (L*H);
        cout << "porosity: " << porosity << endl;
```

```
char buff[1024];
char next[100];
int numrow;

FILE *fin, *fout;

char string_change[1000];

int file_num=0;
int * time = new int [20000];

int IX;

struct _finddata_t c_file;
long hFile;

////////////////////////////
////////////// Gathering data for calculation...
////////////////////////////
// Pressure data for high-flow simulation
file_num=0;
if( (hFile = _findfirst( "hi__gathered_cycle_pressure_vol_avg.txt",
        &c_file )) == -1L ){
        printf( "No files in current directory!\n" );
}
else{
        printf( "Listing of files\n" );
```

```
do{
        numrow=0;
        printf( " %-12s\n",c_file.name);
        fin = fopen(c_file.name,"r");

        ifstream inpfile(c_file.name);
    char next[80];
         while (inpfile)
          {
                if (numrow % 2 == 0){
                        inpfile.getline(next, 80);
                        fscanf(fin, "%d %lf %lf %lf %lf %lf %lf",
                        &dummy1,&p_1_hi[numrow/2],
                        &p_2_hi[numrow/2],&p_3_hi[numrow/2],
                        &p_4_hi[numrow/2],  &p_5_hi[numrow/2],
                        &p_6_hi[numrow/2]);
                }

                else {
                         fscanf(fin, "%d %lf %lf %lf %lf %lf %lf",
                        &dummy1,&dummy2, &dummy2,&dummy2,
                        &dummy2,&dummy2,&dummy2);
                }
                numrow = numrow+1;

        }
        file_num = file_num+1;
```

```
                fclose(fin);
        }while( _findnext( hFile, &c_file ) == 0 );
_findclose( hFile );
}

ofstream outfile3333("__hi_press_vol_avg.txt");
for (IX=0; IX<=404; IX++){
                outfile3333 << IX << " " << p_1_hi[IX] << " " <<
                        p_2_hi[IX] <<" " <<
                        p_3_hi[IX] <<" " <<
                        p_4_hi[IX] <<" " <<
                        p_5_hi[IX] <<" " <<
                        p_6_hi[IX] <<endl;
}
cout << endl;

// Velocity data for high-flow simulation
file_num=0;
if( (hFile = _findfirst( "hi__gathered_cycle_velocity_vol_avg.txt",
        &c_file )) == -1L ){
        printf( "No files in current directory!\n" );
}
else{
        printf( "Listing of files\n" );
        do{
                numrow=0;
                printf( " %-12s\n",c_file.name);
```

```
        fin = fopen(c_file.name,"r");

        ifstream inpfile(c_file.name);
    char next[80];
         while (inpfile)
          {
                if (numrow % 2 == 0){
                      inpfile.getline(next, 80);
                      fscanf(fin, "%d %lf %lf %lf %lf %lf %lf %lf",
                      &dummy1, &vel_inlet_hi[numrow/2],
                      &u_1_hi[numrow/2], &u_2_hi[numrow/2],
                      &u_3_hi[numrow/2], &u_4_hi[numrow/2],
                      &u_5_hi[numrow/2],&u_6_hi[numrow/2]);
                }

                else {
                       fscanf(fin, "%d %lf %lf %lf %lf %lf %lf %lf",
                            &dummy1,&dummy2,&dummy2,
                    &dummy2,&dummy2,&dummy2,&dummy2,&dummy2);
                }
                numrow = numrow+1;

        }
        file_num = file_num+1;

        fclose(fin);
}while( _findnext( hFile, &c_file ) == 0 );
```

```
_findclose( hFile );
}

ofstream outfile33332("__hi_vel_vol_avg.txt");
for (IX=0; IX<=404; IX++){
                outfile33332 << IX << " " << vel_inlet_hi[IX] << " " <<
                        u_1_hi[IX] <<" " <<
                        u_2_hi[IX] <<" " <<
                        u_3_hi[IX] <<" " <<
                        u_4_hi[IX] <<" " <<
                        u_5_hi[IX] <<" " <<
                        u_6_hi[IX] <<endl;
}
cout << endl;

// Pressure data for low-flow simulation
file_num=0;
if( (hFile = _findfirst( "low__gathered_cycle_pressure_vol_avg.txt",
        &c_file )) == -1L ){
        printf( "No files in current directory!\n" );
}
else{
        printf( "Listing of files\n" );
        do{
                numrow=0;
                printf( " %-12s\n",c_file.name);
                fin = fopen(c_file.name,"r");
```

```
                ifstream inpfile(c_file.name);
            char next[80];
                 while (inpfile)
                  {
                        inpfile.getline(next, 80);
                              fscanf(fin, "%d %lf %lf %lf %lf %lf %lf",
                               &dummy1,&p_1[numrow],
                              &p_2[numrow],&p_3[numrow],&p_4[numrow],
                              &p_5[numrow],&p_6[numrow]);
                        numrow = numrow+1;
                  }
                  file_num = file_num+1;


                  fclose(fin);
          }while( _findnext( hFile, &c_file ) == 0 );
_findclose( hFile );
}

ofstream outfile33331("__low_press_vol_avg.txt");
for (IX=0; IX<=404; IX++){
                  outfile33331 << IX << " " << p_1[IX] << " " <<
                        p_2[IX] <<" " << p_3[IX] <<" " <<
                        p_4[IX] <<" " << p_5[IX] <<" " <<
                        p_6[IX] <<endl;
}
cout << endl;
```

```
// Velocity data for low-flow simulation
file_num=0;
if( (hFile = _findfirst( "low__gathered_cycle_velocity_vol_avg.txt",
        &c_file )) == -1L ){
        printf( "No files in current directory!\n" );
}
else{
        printf( "Listing of files\n" );
        do{
                numrow=0;
                printf( " %-12s\n",c_file.name);
                fin = fopen(c_file.name,"r");

                ifstream inpfile(c_file.name);
            char next[80];
                 while (inpfile)
                  {
                        inpfile.getline(next, 80);
                        fscanf(fin, "%d %lf %lf %lf %lf %lf %lf %lf", &dummy1,
                                &vel_inlet[numrow],&u_1[numrow],
                                &u_2[numrow],&u_3[numrow],&u_4[numrow],
                                &u_5[numrow],&u_6[numrow]);
                        numrow = numrow+1;
                }
                file_num = file_num+1;

                fclose(fin);
```

```
        }while( _findnext( hFile, &c_file ) == 0 );
_findclose( hFile );
}

ofstream outfile333313("__low_vel_vol_avg.txt");
for (IX=0; IX<=404; IX++){
                outfile333313 << IX << " " << vel_inlet[IX] << " " <<
                        u_1[IX] <<" " << u_2[IX] <<" " <<
                        u_3[IX] <<" " << u_4[IX] <<" " <<
                        u_5[IX] <<" " << u_6[IX] <<endl;
}
cout << endl;

//////////////////////////////
////////////// FDM simulation...
//////////////////////////////
for (N=2; N<=402; N=N+1){
        Re[N] = rho * porosity * u_5[N] * L / vis;
}

for (N=2; N<=402; N=N+1){
        Re_hi[N] = rho * porosity * u_5_hi[N] * L / vis;
}

bf1_avg = 0;
Kf1_avg = 0;
```

```
//// Low-flow simulation for permeability coefficient
for (N=2; N<=402; N=N+1){
        // conservative second-order central difference for convection term
        left_term[N] = rho * ( (u_5[N]-u_5[N-1])/time_step
                + (u_6[N]*u_6[N]-u_4[N]*u_4[N])/L/4. );

        // nonconservative second-order central difference for convection term
        left_term[N] = rho * ( (u_5[N]-u_5[N-1])/time_step
                + u_5[N]*(u_6[N]-u_4[N])/L/2. );

        press_term[N] = -1.* (p_6[N] - p_4[N])/L/2.;
        vis_term[N] = vis* ( u_6[N] - 2.*u_5[N] + u_4[N] ) / L / L;

        Kf1[N] = (press_term[N] - left_term[N] + vis_term[N]
                - porosity*porosity*rho*bf1_avg/L*u_5[N]*u_5[N]) * L * L
                / vis / (porosity * u_5[N]);
        if (N>=202){
                Kf1_avg = Kf1_avg + Kf1[N];
        }
}

Kf1_avg = Kf1_avg / 201.;

//// High-flow simulation for Forchheimer coefficient
bf1_avg = 0;
for (N=2; N<=402; N=N+1){
        // conservative second-order central difference for convection term
```

```
left_term_hi[N] = rho * ( (u_5_hi[N]-u_5_hi[N-1])/time_step
                    + (u_6_hi[N]*u_6_hi[N]-u_4_hi[N]*u_4_hi[N])/L/4. );

// nonconservative second-order central difference for convection term
left_term_hi[N] = rho * ( (u_5_hi[N]-u_5_hi[N-1])/time_step
                + u_5_hi[N]*(u_6_hi[N]-u_4_hi[N])/L/2. );

// nonconservative first-order upwind difference for convection term
left_term_hi[N] = rho * ( (u_5_hi[N]-u_5_hi[N-1])/time_step
                    + u_5_hi[N]*(u_5_hi[N]-u_4_hi[N])/L );

// nonconservative second-order upwind difference for convection term
left_term_hi[N] = rho * ( (u_5_hi[N]-u_5_hi[N-1])/time_step
                    + (3.*u_5_hi[N]-4.*u_4_hi[N]+u_3_hi[N])/L/2. );

// nonconservative third-order upwind difference for convection term
left_term_hi[N] = rho * ( (u_5_hi[N]-u_5_hi[N-1])/time_step
                    + (2.*u_6_hi[N]+3.*u_5_hi[N]
                    -6.*u_4_hi[N]+u_3_hi[N])/L/6. );

press_term_hi[N] = -1.* (p_6_hi[N] - p_4_hi[N])/L/2.;
vis_term_hi[N] = vis* ( u_6_hi[N] - 2.*u_5_hi[N] + u_4_hi[N] ) / L / L;

bf1[N] = (press_term_hi[N] - left_term_hi[N] + vis_term_hi[N])
            *L/rho/(porosity * u_5_hi[N])/(porosity * u_5_hi[N])
                - Kf1_avg/Re_hi[N];
```

```
        if (N>=202){  bf1_avg = bf1_avg + bf1[N]; } }
        bf1_avg = bf1_avg / 201.;

        cout << endl;
        cout << "Kf1_avg: " << Kf1_avg << "    ";
        cout << "bf1_avg: " << bf1_avg << endl;
        getch();

////////////////////////////////////////////////////////////////////
// write data file
        ofstream outfile1236("___cycle_results.txt");
        outfile1236 << "N   Re[N]   left_term[N]   press_term[N]   vis_term[N]
                Re_hi[N]   left_term_hi[N]   press_term_hi[N]   vis_term_hi[N]
                Kf1[N]   bf1[N]" << endl;
        outfile1236 << "L^2/Kf1_avg" << endl;
        outfile1236 << "bf1_avg*L" << endl;
        for (N=2; N<=402; N=N+1){
                outfile1236 << N << " " << Re[N] << " " << left_term[N] << " " <<
                                press_term[N] << " " << vis_term[N] << " " <<
                                Re_hi[N] << " " << left_term_hi[N] << " " <<
                                press_term_hi[N] << " " << vis_term_hi[N] << " " <<
                                Kf1[N] << " " << bf1[N] << " " << endl;
        }
        outfile1236 << "Kf1_avg" << Kf1_avg << endl;
        outfile1236 << "bf1_avg" << bf1_avg << endl;
        getch();
}
```

REFERENCES

[1] Harvey, J. P., "Oscillatory compressible flow and heat transfer in porous media - application to cryocooler regenerators," Ph.D. thesis, Georgia Institute of Technology, Atlanta, GA, 2003.

[2] Vafai, K., and Tien, C.L., "Boundary and inertia effects on flow and heat transfer in porous media," Int. J. Heat Mass Transfer, Vol. 24, pp. 195-203, 1981.

[3] Hsu, C. T., and Cheng, P., "Thermal dispersion in a porous medium," Int. J. Heat Mass Transfer, Vol. 33, pp.1587-1597, 1990.

[4] Liu, S., Afacan, A., and Masliyah, J., "Steady incompressible laminar flow in porous media," Chemical Engineering Science, Vol. 49, pp. 3565-3586, 1994.

[5] Coulaud, O., Morel, P., and Caltagirone, J. P., "Numerical modelling of nonlinear effects in laminar f1low through a porous medium," J. Fluid Mech., Vol. 190, pp. 393-407, 1988.

[6] Amiri, A., and Vafai, K., "Analysis of dispersion effects and non-thermal equilibrium, non-Darcian, variable porosity incompressible flow through porous media," Int. J. Heat Mass Transfer, Vol. 37, pp. 939-954, 1994.

[7] Nakayama, A., "PC-aided numerical heat transfer and convective flow," CRC Press, 1995.

[8] Ochoa-Tapia, J. A., and Whitaker, S., "Momentum transfer at the boundary between a porous medium and a homogeneous fluid-1.Theoretical development," Int. J. Heat Mass Transfer, vol. 38, pp.2635-2646, 1995.

[9] Kaviany, M., "Principles of heat transfer in porous media," 2nd ed., Springer-Verlag, 1995.

[10] Nield, D. A., and Bejan, "Convection in Porous Media," 3rd ed., Springer-Verlag, 2006.

[11] Whitaker, S., "The Method of volume averaging," Kluwer Academic, 1999.

[12] Vafai, K., and Amiri, A., "Non-Darcian effects in confined forced convective flows," D.B. Ingham & I. Pop, Transport Phenomena in Porous Media, Pergamon, pp. 313-329, 1998.

[13] Nakayama, A., Kuwahara, F., and Kodama, Y., "An equation for thermal dispersion flux transport and its mathematical modelling for heat and fluid flow in a porous medium," J. Fluid Mech., Vol. 563, pp. 81-96, 2006.

[14] Nakayama, A., and Kuwahara, F., "A macroscopic turbulence model for flow in a porous medium," J. Fluids Engineering., Vol. 121, pp.427-433, 1999.

[15] Kuwahara, F., Shirota, M., and Nakayama, A., "A numerical study of interfacial convective heat transfer coefficient in two-energy equation model for convection in porous media," Int. J. Heat Mass Transfer, Vol. 44, pp. 1153-1159, 2001.

[16] Pedras, M.H.J., and De Lemos, M.J.S, "Macroscopic turbulence modeling for incompressible flow through undeformable porous media," Int. J. Heat Mass Transfer, Vol. 44, pp. 1081-1093, 2001.

[17] Nakayama, A., Kuwahara, F., Umemoto, T., and Hayashi, T., "Heat and fluid flow within an anisotropic porous medium," J. Heat Transfer, Vol. 124, pp. 746-753, 2002.

[18] Sahiti, N., Lemouedda, A., Stojkovic, D., Durst, F., and Franz, E., "Performance comparison of pin fin in-duct flow arrays with various pin cross-sections," Applied Thermal Engineering, Vol. 26, pp. 1176-1192, 2006.

[19] Sara, O. N., "Performance analysis of rectangular ducts with staggered square pin fins," Energy Conversion and Management, Vol. 44, pp. 1787-1803, 2003.

[20] Jang, J. Y., Lai, J. T., Liu, L. C., "The thermal-hydraulic characteristics of staggered circular finned-tube heat exchangers under dry and dehumidifying condition," Int. J. Heat Mass Transfer, Vol. 41, pp. 3321-3337, 1998.

[21] Kim, D., Kim, S. J., and Ortega, A., "Compact modeling of fluid flow and heat transfer in pin fin heat sinks," J. Electronic Packaging , Vol. 126, pp. 342-350, 2004.

[22] Jeng, T. M., and Tzeng, S. C., "A semi-empirical model for estimating permeability and inertial coefficient of pin-fin heat sinks," Int. J. Heat Mass Transfer, Vol. 48, pp. 3140-3150, 2005.

[23] Lage, J. L., and Antohe, B. V., "Darcy's experiments and the deviation to nonlinear flow regime," J. Fluids Engineering, Vol. 233, pp. 619-625, 2000.

[24] Fluent INC., Fluent 6 User Manual, 2006.

[25] Fluent INC., Gambit 2 User Manual, 2006.

[26] Benarji, N., Balaji, C., and Venkateshan, S. P., "Unsteady fluid flow and heat transfer over a bank of flat tubes," Heat Mass Transfer, DOI 10.1007/s00231-007-0256-5, 2007.

[27] Raju, K. S., and Narasimhan, A., "Porous medium interconnector effects on the thermohydraulics of near-compact heat exchangers treated as porous media," J. Heat Transfer, Vol. 129, pp. 273-281, 2007.

[28] Panfilov, M., and Fourar, M., "Physical splitting of nonlinear effects in high-velocity stable flow through porous media," Advances in Water Resources, Vol. 29, pp. 30-41, 2006.

[29] Lucas, Y., Panfilov, M., and Bues, M., "High velocity flow through fractured and porous media: the role of flow non-periodicity," European J. Mech. B/Fluids, Vol. 26, pp. 295-303, 2007.